Karlsruhe Institute of Technology

KSOP Karlsruhe School of Optics & Photonics

Investigation of the influence of the sample topography on the measurement uncertainty of a scanning white light interferometer

Master Thesis
in Optics and Photonics
handed in by

Adapa Bharath Reddy

The Master Thesis was conducted at the
Fraunhofer IPMS under the supervision of

Dr. rer. nat. Christoph Skupsch (IPMS)

and

Prof. Dr. rer. nat. Uli Lemmer (KIT)

September 2016

Declaration

I hereby declare that I wrote my Master's Thesis on my own and that I have followed the regulations relating to good scientific practice of the Karlsruhe Institute of Technology (KIT) in its latest form. I did not use any unacknowledged sources or means and I marked all references I used literally or by content.
Date: 27/09/2016
A. Bharath Reddy

Contents

List of Figures v

Glossary viii

Abstract ix

1. Introduction 1

1.1 Scanning White Light Interferometry 1

1.1.2 Optical Principles 3

1.1.3 WLI adjustment 8

1.1.4 Topography computation 9

1.1.5 Measurement Uncertainty 12

1.2 Micromirror Arrays 14

1.2.1 Structure 14

1.2.2 Applications 15

2. Experimental and Analysis Methods 18

2.1 WLI Adjustment 19

2.2 Samples 24

2.3 Sample Cover 28

2.4 Raw Data Analysis 29

2.4.1 Phase uncertainty 32

2.4.2 Height uncertainty 32

2.4.3 Measured Roughness 33

3. Results and Discussion 34

3.1 Tilted SiC Standard 35

3.1.1 Aberrations 35

3.1.2 WLI Adjustment 36

3.1.3 Sample Cover 39

3.1.4 Theoretical Estimations 41

3.2 Tilted Micromirrors 43

3.2.1 Topography Measurements 43

3.2.2 Measurement Uncertainty 45

3.2.3 Field of view (FOV) 47

4. Conclusions 50

4.1 Prediction of Measurement Accuracy 50

4.2 Influence of Sample Coverage 50

4.3 Influence of WLI Adjustment 51

4.4 Gain for Micromirror Characterization 52

4.5 Outlook 52

Appendix 53

References 56

List of Figures

FIGURE 1.1 Sketch of Scanning White Light Interferometer 2

FIGURE 1.2 Michelson interferometric setup 3

FIGURE 1.3 Interference microscopy objectives 4

FIGURE 1.4 Interferometric patterns superimposed at different wavelengths 5

FIGURE 1.5 Schematic of building up correlograms over a surface 6

FIGURE 1.6 a. Spectral density function of light source b. Intensity correlogram as a function of sample scan position 7

FIGURE 1.7 a. Optical ray path for a flat adjustment surface 8

FIGURE 1.7 b. Optical ray path for a tilted adjustment surface 9

FIGURE 1.8 A basic interferometric setup 10

FIGURE 1.9 Linear fitting the phase with spatial frequencies 11

FIGURE 1.10 A hexagonal micro-mirror used for Laser Direct Imaging applications 14

FIGURE 1.11 Mirror deflection as a function of mirror driving voltage 14

FIGURE 1.12 a. sketch of actuator layout with three layers: hinge, hinge reinforcement and mirror, b. SEM image of MMA in close up 15

FIGURE 1.13 WLI image of deflected micromirrors (height exaggerated) 15

FIGURE 1.14 History of illumination source shapes 16

FIGURE 1.15 Changing illumination shape by tilting mirrors 16

FIGURE 1.16 Moiré fringe pattern created by superposition of structured illumination and sample structure 17

FIGURE 1.17 Selected illumination sketch on a biological sample 17

FIGURE 2.1 A picture of Zygo New View 7300 WLI used for our experiments. MetroPro software is displayed in one monitor and a live display available on a second monitor 18

FIGURE 2.2 MetroPro surface analysis screenshot obtained from MetroPro manual 19

FIGURE 2.3 WLI adjustment with MMA X-tilt, unidirectional pattern 20

FIGURE 2.4 Correlogram recorded at a random CCD pixel 21

FIGURE 2.5 Zygo NV7300 common adjustment features 22

FIGURE 2.6 F-Stop closed to maximum and the system is in focus 22

FIGURE 2.7 Reference path adjustment with phase wedge and reference 23

FIGURE 2.8 a. WLI head tilt with respect to sample surface normal, b. Optical path of central ray 24

FIGURE 2.9 Height topography of SiC mirror when WLI head is tilted 1.7° along X-axis. The experiment performed without any sample cover glass 25

FIGURE 2.10 Tilted sample (relative to WLI head) have regions in FOV outside scan range 25

FIGURE 2.11 a. Height topography of MEMI surface with mirrors tilted ±1.8° Y-axis, b. Topography in small region of interest 26

FIGURE 2.12 MEMI mirrors are in scan range even at large tilts 27

FIGURE 2.13 Recognized mirrors on MEMI MMA 27

FIGURE 2.14 Optical setup difference in presence of a cover glass for a. SiC mirror and b. MEMI samples 28

FIGURE 2.15 Correlogram signal with DC component I_0 30

FIGURE 2.16 Sample beam collection loss for tilted sample 30

FIGURE 2.17 Phase function obtained from our matlab FDA analysis 31

FIGURE 3.1 Aberrations in SiC mirror height measurement data 35

FIGURE 3.2 Measured roughness (MR) with and without aberration correction 36

FIGURE 3.3 a. Mean height uncertainty (δh_m) and b. Std in height uncertainty (δh_{std}) for different tilts, adjustments and no sample coverage 37

FIGURE 3.4 Measured roughness errorbars for different tilts, adjustments and no sample coverage 37

FIGURE 3.5 a. Mean height uncertainty (δh_m) and b. Std in height uncertainty (δh_{std}) for different tilts, adjustments and 3 mm CG 38

FIGURE 3.6 a. Mean measured roughness (MR_m) and b. Std in measured roughness (MR_{std}) for different tilts, adjustments and 3 mm CG 39

FIGURE 3.7 a. Mean height uncertainty (δh_m) and b. Std in height uncertainty (δh_{std}) for different tilts and No/1.6mm/3mm CG 40

FIGURE 3.8 a. Mean measured roughness (MR_m) and b. in measured roughness (MR_{std}) for different tilts and No/1.6mm/3mm CG 40

FIGURE 3.9 Theory and experimental results comparison for different sample coverage and different WLI adjustments 42

FIGURE 3.10 Measured roughness comparison between MetroPro and our IPMS results 42

FIGURE 3.11 MEMI sample topography @ 0° mirror tilt 43

FIGURE 3.12 MEMI in a ROI of 7x7 mirrors tilted @ 3.2° a. Mirrors pixel-wise, b. Mirrors fit to plane 44

FIGURE 3.13 Height uncertainty (δh) pixel-wise in ROI 46

FIGURE 3.14 a. Height uncertainty (δh) errorbars over ROI (pixel-wise), b. δh errorbars over FOV (pixel-wise) 46

FIGURE 3.15 a. Measured roughness (MR) errorbars over ROI (mirror-wise), b. MR errorbars over FOV (mirror-wise) 47

FIGURE 3.16 a. Height uncertainty (δh) mirror-wise for MEMI mirror tilts at 1.07° and b. mirror tilts at 3.2° 47

FIGURE 3.17 a. Mirror wise height uncertainty (δh) radial distributions separately for [+Y] and [-Y] tilts at 1.07° and b. linear fit of the δh radial distributions 48

FIGURE 3.18 Mean DC intensity of correlograms recorded in FOV 49

Glossary

SWLI	- Scanning White Light Interferometry
MOEMS	- Micro-opto-electro-mechanical systems
SiC	- Silicon Carbide
CCD	- Charge Coupled Device
FDA	- Frequency Domain Analysis
FFT	- Fast Fourier Transform
λ	- Wavelength
k	- Wavenumber (1/λ) or spatial frequency
k_{ph}	- Physically present spatial frequency in light source
std	- Standard Deviation
$\phi_{res}(\mathrm{k})$	- Linear phase fit residuals as a function of spatial frequency
$\delta\phi_{pix}$	- Phase residual of a pixel
δh_{pix}	- Height residual of a pixel
$\delta\phi_m$(δh_m)	- Phase (height) uncertainty mean
$\delta\phi_{std}$(δh_{std})	- Phase (height) uncertainty standard deviation
MR_m	- Measured roughness mean
MR_{std}	- Measured roughness standard deviation
ROI	- Region of Interest
FOV	- Field of View
OPD	- Optical path difference
CG	- Cover Glass
Syserr	- System error data
DOE	- Diffractive optical elements
WLIC	- Interference contrast of WLI at zero OPD

Abstract

Scanning White Light Interferometry (SWLI) is used for time-effective three-dimensional topography measurements on micro-opto-electro-mechanical systems (MOEMS), like micromirror arrays. The typical resolution is about 1µm laterally and about 1nm in height. The latter is only true for flat, smooth surfaces. The uncertainty budget of a SWLI measurement on a MOEMS not only contains the aberrations of the instrument´s optics. It also includes at least two further sources: surface and cover glass effects. In this work both effects are investigated experimentally by measuring the performance of an SWLI in dependence on surface tilt and cover glass thickness. The SWLI performance is estimated by two individual measures. First, the phase uncertainty resulting from a self-made frequency domain analysis (FDA) of the measured intensity stack is evaluated. Second, the measured roughness of the sample under test is determined. Comparison of experiments with theory reveals appropriate adjustment and removing the cover leads to better than expected performance.

It is well known that the height uncertainty increases for increasing surface gradients. SWLI measurements on tilted micro-mirrors are less precise than measuring flat ones. One countermeasure against that is an appropriate SWLI adjustment. In this work we show that adjustment with specialized surfaces can lead to significantly reduced height uncertainty for tilted surfaces. Results obtained with a silicon carbide (SiC) standard are translated to measurements on MOEMS.

Cover glasses may increase height uncertainty. A cover is often used, as MOEMS are purged with an inert gas during operation to minimize corrosion effects. Three different cover cases are analyzed. We show the absence of any cover glass yields minimum measured roughness and phase uncertainty. The latter increases with cover glass thickness.

The most important findings of this thesis: A) Using thinner cover glass reduces height uncertainty. This may be beneficial for advanced SWLI algorithms as provided by the Zygo corp. B) Using special surfaces for SWLI adjustment can reduce height uncertainty. The adjustment surface should be as similar as possible to the surface to be measured. C) Theoretical prediction of the height uncertainty for particular surface tilts is mostly unfeasible. The theoretical model needs adaption for micromirror characterization.

Chapter 1

Introduction

1.1 Scanning White Light Interferometry

Optical interferometric techniques are commonly used for testing deformations on mechanical surfaces using optical non-contact methods. These techniques are very useful especially for the characterization of micro (opto) electro-mechanical systems (M(O)EMS). The optical interference techniques combined with microscopy can profile surfaces with sub-nanometer height precision and sub-micron lateral resolutions [15].

White Light Interferometer (WLI) or more specifically Vertical Scanning White Light Interferometer (SWLI) is most extensively used as an optical profiler in surface metrology for high-precision industrial applications [15]. Some of the advantages of the SWLI are given in the following.

- SWLI uses white light source for interference. White light can remove the phase ambiguities raised, in case of a single wavelength light interferometry like Phase Shifting Interferometry.
- SWLI can perform a fast lateral scanning with relatively large field of view.
- SWLI measures surface profile with high precision in nanometer range, much smaller than the mean optical wavelength (hundreds of nm) and the mechanical scan steps (tens of nm) in Z-direction.
- SWLI can measure a 3D surface map with no contact to the surface and has no wearable parts that need replacement, unlike some contact profilers (stylus profiler) [16].

The following sections will describe the components of a WLI (hardware), its principles of operation and the computations of topography. We focus on the measurement uncertainties arising from the topography computations, as the WLI precision is reflected in the statistical analysis of topography measurements.

1.1.1 Hardware

Different components of a WLI are shown in figure 1.1. The WLI can be divided into three sections: (a) *Illumination*, (b) *Interference microscopy* and (c) *Imaging*.

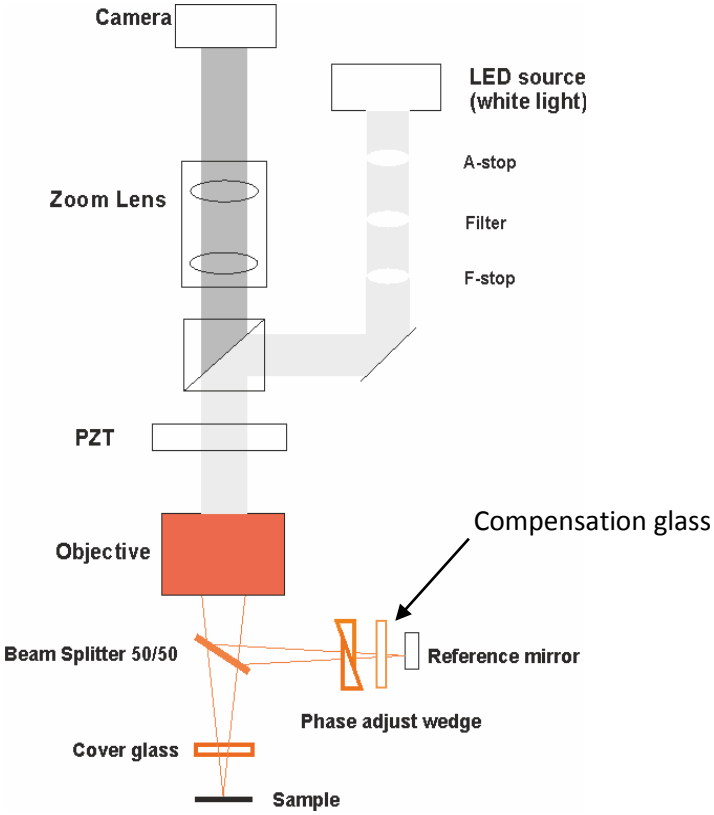


FIGURE 1.1 Sketch of Scanning White Light Interferometer

a. WLI illumination

WLI uses a white light source usually an LED source. The LED source does not generate true white light as in wavelengths in the whole range of visible spectrum. It has bandwidth of some tens of nanometers. The LED source is selected based on its central wavelength, coherence length and the light power needed. Aperture stop (A-stop) limits the amount of light illumination. Field stop (F-stop) limits the field of view and we can use it as focus aid. And we use filter if necessary to change the spectral bandwidth (and this in turn changes coherence length) [14].

b. Interference microscopy

The illumination beam is split into two equal halves by a beam splitter. One half of the beam is reflected by the sample and the other half is reflected by a reference mirror. They combine and pass through a microscope objective. If the separation in the path lengths of the two identical beams is within the coherence length, the beams after combination produce an interference pattern (interferogram) [15, 16].

We place a cover glass over the sample for protection and a compensation glass is placed in the reference beam path. It compensates the phase added (or more precisely the optical path) in the sample beam through cover glass.

c. Imaging

A piezo translator (PZT) is used between the microscope objective and the illumination system. We can translate the piezo in steps (i.e. scanning) and create a phase modulation vertical to the sample in the combined beam. A CCD camera is used to record the interferogram. A field zoom lens is used before the camera which we can use to further magnify the image on camera (apart from the magnification of microscope objective) [14].

We record a different interferogram for each pixel. When combined over all pixels the total interferometric data contains (a) 2D lateral phase information of the sample and (b) the vertical phase modulation [16].

1.1.2 Optical Principles

A typical WLI device uses Michelson interferometric setup as shown in figure 1.2.

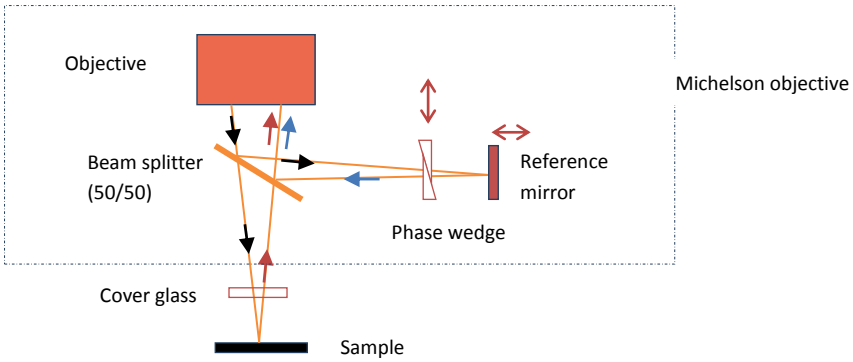


FIGURE 1.2 Michelson interferometric setup [25]

Michelson objective (in figure 1.2) uses microscope objective with Michelson two-beam interferometric setup. Light illumination is split into two beams by a beam splitter. The two beams are focused on the sample and reference mirror, and they are reflected back. Optical path difference (OPD) between the two beams creates the generally observed interference patterns. The OPD is reflected in the phase difference (ϕ) between the beams, given by

$$\phi = \frac{2\pi\,(2L)}{\lambda} \qquad \text{(Eq1.1)}$$

where 2L is the OPD. Here L is the difference in arm lengths, light in each arm is reflected and travels twice the distance. And λ is the wavelength, here only a single wavelength (small linewidth) in the beam is presented. For multiple wavelengths like in the case of white light, phase is separately defined for each wavelength and the interference pattern is derived from the superimposition of interference at all wavelengths [1], as described in the following.

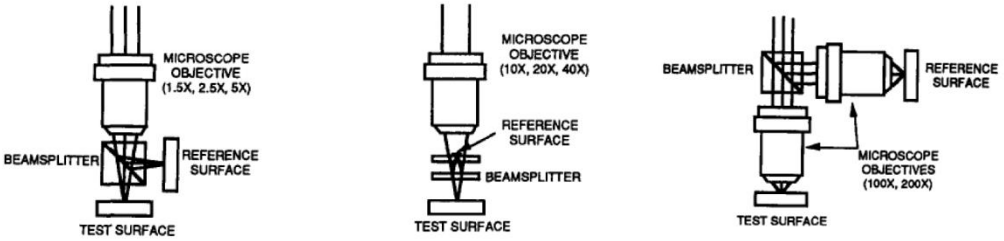
Reflected sample beam carries the phase front of sample surface which contains the height information. A smooth reference mirror is selected so that the reflected reference beam has planar phase front. The two beams when combined forms interference pattern which can be recorded by CCD camera. The interference intensity I(x,y) is given by

$$I(x,y) = I_0(1 + V\,cos(\phi(x,y,L) + \phi_0)) \qquad \text{[8, 15] (Eq 1.2)}$$

where I_0 is the sum of intensities of two beams ($I_0 = I_1 + I_2$),
$V = \frac{2\sqrt{I_1 I_2}}{I_1 + I_2}$ is the visibility,
$\phi(x,y,L)$ is the phase difference between the two beams, note that L (difference in arm lengths) is measured with a reference sample plane (Z=0 plane). Height variation on sample surface changes OPD. And ϕ_0 is the additional phase from the light reflections by mirrors.

In addition to Michelson objective, Mirau and Linnik objectives are commonly used depending on the application.

Microscope objectives:



a. Michelson objective **b.** Mirau objective **c.** Linnik objective

FIGURE 1.3 Interference microscopy objectives [3]

The Michelson objective (figure 1.3a) is used for low magnifications such as 1.5X, 2.5X and 5X [3]. Here only a single objective is used. Objective sends the incidence beam and collects the interference beam from the michelson interferometer setup. As the beam splitter is placed between the sample and the objective, only long working distance objectives can be used.

The Mirau objective (figure 1.3b) is used for medium magnifications such as 10X, 20X and 40X [3]. Similar to michelson objective a single objective with long working distance is used. Reference mirror is placed along the objective optical axis which may obstruct some portion of the beam, but it is

insignificant at medium magnifications (size of reference mirror is similar to field of view size on sample).

The Linnik objective (figure 1.3c) is used for high magnifications such as 100X and 200X [3]. Major disadvantage is that two matched objectives are needed. However as the objectives can be placed close to sample surface (and reference), large numerical apertures and short working distances can be used. In addition large numerical apertures are used which allowsfinest resolutions.

Interference with multi-wavelength sources (white light):

We process the recorded interferogram to first resolve the phase information, and from which we obtain the height information of the sample surface. Light sources with single wavelength (e.g. lasers with very small linewidth) can produce interference pattern within a large range of optical path differences, due to their large coherence length. But the white light sources have a limited range of OPD to have interference, as explained in the figure 1.4.

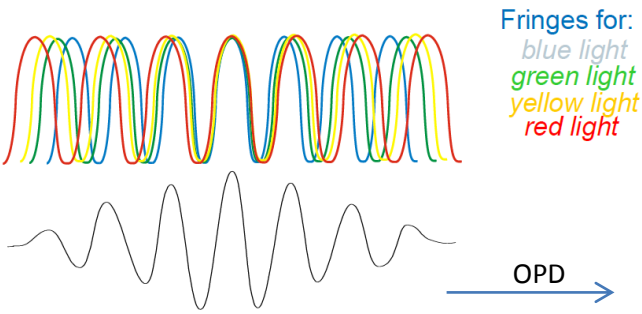


FIGURE 1.4 Interferometric patterns superimposed at different wavelengths [1]

As shown in the figure 1.4 each wavelength has a different phase modulation (see Eq 1.1) and different interference patterns. But they all overlap constructively when optical path difference (OPD) is zero. When we move away from zero OPD the phase relation between wavelengths gets complex and the interference is lost. Beyond the coherence length no well-defined phase relation can be derived between the two beams, and thus no interference pattern appears [17]. Note that the interferogram in the figure 1.4 is usually derived after multiple scans (above and below OPD=0) at a single pixel on the sample. This interferogram is also referred as correlogram by the WLI community.

Visibility of the interference reduces as we scan away from the zero OPD (we get zero OPD when the arm lengths of the (Michelson) interferometer are equal (i.e. L=0). This factor usually implies harder alignment of interferometer with white light source but certain advantages (as shown below) makes white light more preferable compared to single wavelength interferometry.

- Interference contrast reaches maximum at the center of correlogram when OPD is 0. Correlograms are obtained separately for all the pixels. Correlogram can be analyzed to precisely find the position for zero OPD [18]. These positions stitched together can generate surface topography.
- For a single wavelength, interference pattern on the sample becomes indistinguishable for a 2π phase shift. A height step larger than $\lambda/4$ on the sample can generate ambiguities. White light sources avoid these 2π phase ambiguities [15].

Correlogram:

WLI device scans along z-direction and records interference intensity. Each pixel acts as a separate interferometer and creates a separate correlogram as illustrated in the figure 1.5.

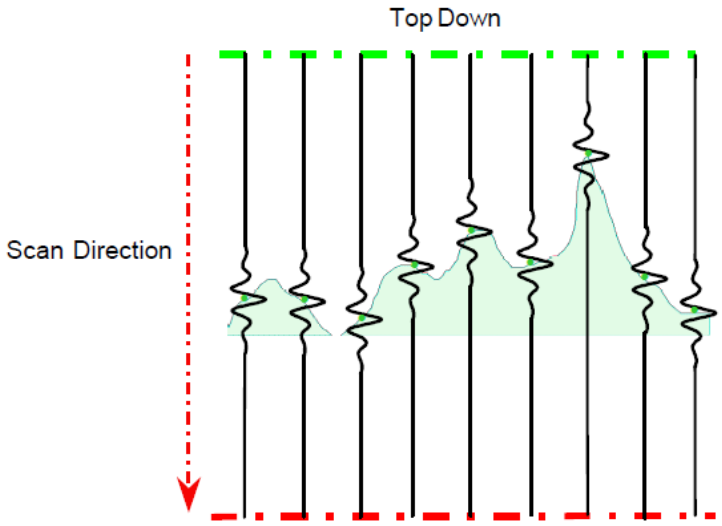


FIGURE 1.5 Schematic of building up correlograms over a surface [4]

When we scan using WLI we change the OPD between the beams and we generate a time delay between the two beams. As the white light has low temporal coherence we get the correlogram patterns in the interference. At exactly zero the optical path difference (OPD), the two beams in the interferometer arms reach the beam-splitter (in return) at exactly same time, and thus have the same phase over all wavelengths (and thus constructively superimpose over all wavelengths). If the beam paths differ more than the coherence length, the visibility V becomes zero (see Eq 1.2) [19].

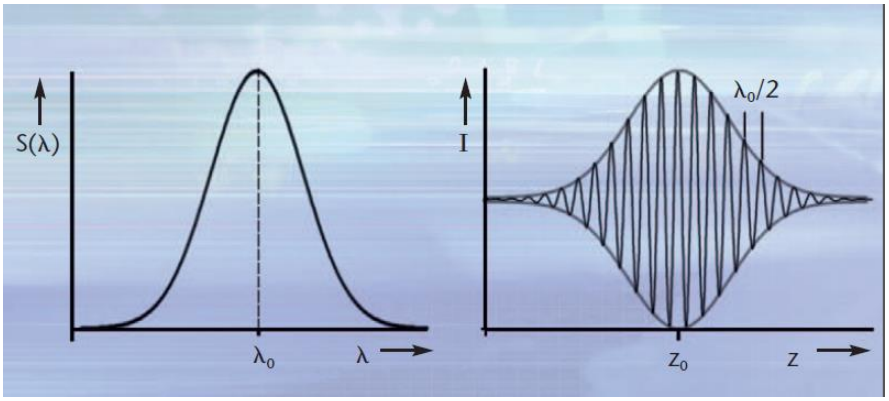


FIGURE 1.6 a. Spectral density function of light source **b.** Intensity correlogram as a function of sample scan position [5]

Correlogram shape and size depends on the spectral distribution of the light source, as seen in figure 1.6a. As shown from figure 1.6b, we can derive four important parameters of the recorded correlogram, which are

Position: The correlogram centers around Z_0 (at OPD=0). This center position corresponds to the maximum contrast. Z_0 is also the relative height of the pixel on the sample surface.

Size: We have maximum intensity of signal at Z_0. We can get two positions (Z_+, Z_-) on either side from Z_0 when intensity drops to 1/e of the maximum value. We define the correlogram length between these two points as

$$L_{cor} = Z_+ - Z_-$$

Intensity drops to 1/e when the OPD is equal to the coherence length L_c. Coherence length is equivalent to OPD at Z_+(or Z_-) position, which is given by

$$OPD = 2(Z_+ - Z_0) = L_{cor}$$

we have a factor 2, as we have the light travels twice the distances in each arm. We can see from the above relations that correlogram length is equal to coherence length (L_c). Coherence length also depends on the spectral bandwidth, as given by

$$L_c = c\,\tau_c \qquad \text{[6] (Eq 1.3)}$$

$$\tau_c \Delta f \approx 1 \qquad \text{[6] (Eq 1.4)}$$

A light source with wider spectral bandwidth (Δf) will have low coherence length and thus create a smaller correlogram.

Shape: The shape of the correlogram depends on spectral density function of the light source. In case of a Gaussian spectral density (common for most LED sources) correlogram will also have Gaussian shaped envelope, as given by

$$I(z) = I_0(1 + \exp\left[-4\left(\frac{z-z_0}{lc}\right)^2\right]\cos(4\pi\frac{z-z_0}{\lambda_0} - \phi_0)) \qquad [5] \text{ (Eq 1.5)}$$

Period: Correlogram fringes are separated by $\lambda_0/2$ where λ_0 is the central wavelength of the light source (see Eq 1.5) [5].

We choose a scan length larger than the correlogram as shown in figure 1.5, and the sample is placed at a plane with equal arm length as the reference mirror. Samples can be scanned over much larger distances than the size of surface features, and scan length is only limited by the mechanical components of WLI. And the WLI can generate correlograms over a large field of view simultaneously and process them, unless the sample is tilted and too big to be in the scan range for whole field of view.

Prior to the measurements the WLI can be adjusted to get the best possible contrast and uniform illumination, over the full field of view on sample. And the WLI may not always use the same surface for both adjustment and measurement.

1.1.3 WLI adjustment

WLI is usually adjusted with a reference surface before measuring with actual sample to minimize the measurement uncertainty. The adjustment not only involves moving the WLI optics but depends on the orientation of the sample as well. As explained in the following, a cover glass over the sample would change the optical path of the sample beam, when the adjustment surface is tilted.

Presence of a cover glass:

In general sample surfaces are covered with a glass for protection. The cover glass increases optical path length of the sample beam as shown in figure 1.7a.

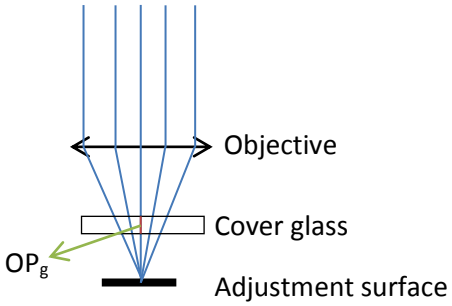


FIGURE 1.7 a. Optical ray path for a flat adjustment surface

Extra optical path (OP_g) is due to the refractive index of the glass. Here we are considering OP_g for the central ray in sample beam.

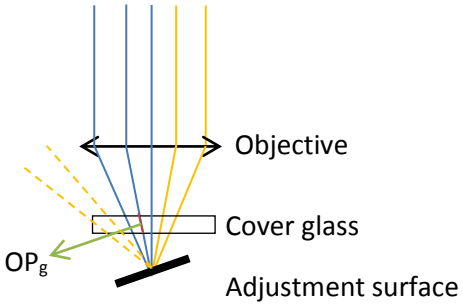


FIGURE 1.7 b. Optical ray path for a tilted adjustment surface

As shown in figure 1.7b the optical path through the glass larger for the tilted adjustment surface. This path can be compensated by adjusting the phase wedge in the reference beam path (see figure 1.2). If the tilts are too large some of incident beam is reflected away from the objective aperture and thus not collected. This might reduce the interference intensity (DC component of interference signal), but it is only observed for large tilts.

1.1.4 Topography computation

Topography of a sample surface can be obtained by analyzing the correlograms. A common procedure used for topography determination is explained in the following.

- Fourier transform correlogram
  - Correlogram signal is recoded in scan steps (i.e. spatial Z-distances). It is Fourier transformed to spatial frequency space (k-space).
- Derive phase as a function of spatial frequency
  - Fourier signal is a complex signal. We can get the phase of the complex signal with simple mathematical calculation as follows

$$I_F(k) = I_R(k) + j\, I_i(k)$$

$$\phi(k) = \tan^{-1}\left(\frac{I_i(k)}{I_R(k)}\right) \qquad \text{(Eq 1.6)}$$

where $I_F(k)$ is the Fourier transformed correlogram intensity with I_R, I_i being the real and imaginary parts,
$\phi(k)$ is the phase as a function of spatial frequency.

- Analyze phase - spatial frequency signal
    - We can get the embedded height information in the phase through phase analysis.

Analysis: Following figure 1.8 shows a general interferometric setup. CCD camera records the interference. I_{out} is recorded by a single CCD pixel. Corresponding pixel P(x, y) in the beam splitter acts as an individual interferometer for sample pixel P'(x,y) and reference pixel P''(x,y). Correlogram is recorded at a pixel P(x,y) by moving the sample plane along z.

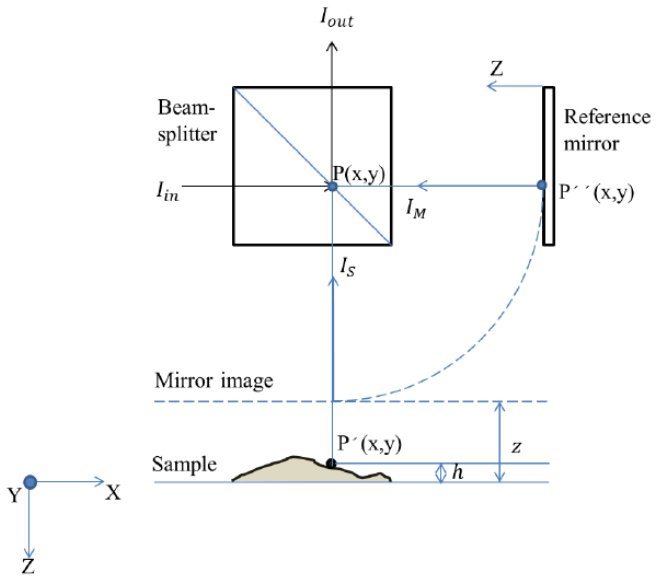


FIGURE 1.8 A basic interferometric setup [8]

We can derive interference intensity at a single wavelength and integrate over all the wavelengths to get the correlogram signal. We can get the OPD between P' and P'' as $2\,[z - h(x,y)]$. We can use two-beam Michelson interference analysis to derive the phase and intensity (from Eq 1.1, 1.2).

Phase and Interference intensity for a single wavelength (λ) is given by

$$\phi(x,y,z,k) = 4\pi k[z - h(x,y)] - \phi_0(x,y,k) \qquad \text{[8](Eq 1.7)}$$

$$I(x,y,z,k) = I_0(1 + V\cos(\phi(x,y,z,k))) \qquad \text{[8] (Eq 1.8)}$$

Where $I_0 = I_1 + I_2$ is the sum of tow beam intensities (DC component),

$V = \frac{2\sqrt{I_1 I_2}}{I_1 + I_2}$ is the visibility,

z is the sample plane from a reference position (z=0 plane),

h(x,y) is the surface height at pixel (x,y),

$\phi_0(x,y,k)$ is the net phase change between reference and sample beams due to reflections at the surface.

We can superimpose the interferences by all the wavelengths present in the light source. And we get

$$I(x,y,z) = \int_{k=-\infty}^{\infty} S(k)\, I_0(1 + V\cos(4\pi k[z - \mathrm{h(x,y)}] - \phi_0))\, \mathrm{dk} \qquad [8]\ (\text{Eq } 1.9)$$

where S(k) is the spectrum of light source. We can integrate over $[-\infty, \infty]$ by setting spectral amplitudes to zero for wavelengths outside the bandwidth. The contrast V is almost a constant for a single wavelength, as it depends only on coherence length and the two beam intensities. We can assume very large coherence length for ideal single wavelength, and assume I_1, I_2 independent of (x,y) position. The integrated intensity takes the correlogram shape shown in figure 1.6b and the contrast varies with z. The envelope of correlogram is determined by the spectral distribution S(k). If S(k) is a Gaussian as in most cases, we get a Gaussian shaped correlogram envelope [5].

We can apply Fourier transform to Intensity (in Eq 1.9) over z to get

$$I_F(x,y,k) = A + \{B\exp(i\,[4\pi k\,\mathrm{h(x,y)} + \phi_0(x,y)]) + CC\} \quad (\text{Eq}1.10)$$

where A is the DC component, B is the spectral intensity, CC is the complex conjugate and the phase is given by

$$\phi(\mathrm{x,y,k}) = 4\pi k\,\mathrm{h(x,y)} + \phi_0(x,y) \qquad [7]\ (\text{Eq } 1.11)$$

For more accurate analysis, dispersion of the system should be considered which makes ϕ_0 change with wavelength i.e. $\phi_0(\mathrm{x,y,k})$. But in many cases dispersion can be corrected as a system error while calibrating WLI.

We can plot the phase (ϕ) as a function of spatial frequency (k) (from Eq 1.11), and we can linear fit the phase – spatial frequency curve within the range of physical wave numbers (i.e. the wavelengths of the light source) as shown in figure 1.9.

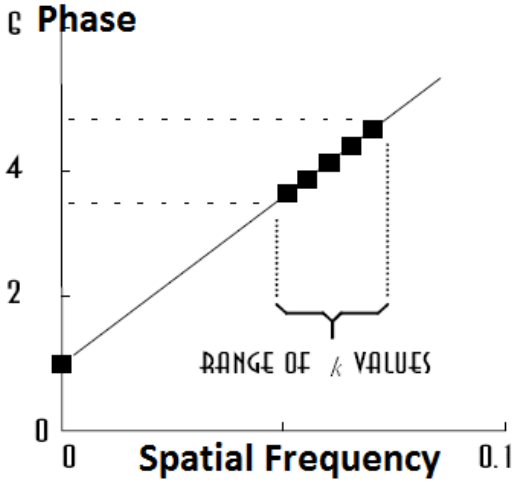


FIGURE 1.9 Linear fitting the phase with spatial frequencies [7]

We can derive the height from slope of the linear fit as

$$slope(\phi, k) = \frac{\Delta\phi}{\Delta \mathrm{k}}$$

$$h(x,y) = \frac{slope\ (\phi,k)}{4\pi} \qquad [7,8] \text{ (Eq 1.12)}$$

1.1.5 Measurement Uncertainty

WLI can measure surfaces to height precision of nanometer scales. The measurements are not limited by the mechanical or optical elements of the WLI system. Measurements are limited by the correlogram analysis. A good WLI adjustment can reduce measurement uncertainty but it does not correct for all the sources of uncertainty, and any deviations from the setup used for adjustment can drastically increase uncertainty. Uncertainty can arise from various sources as explained in the following.

Theoretical analysis of measurement uncertainty:

Measurement uncertainties can vary based on experimental conditions. WLI uses a white light with broad spectrum and as a result it requires highly accurate artifact for calibration/adjustment to reduce systematic errors [20]. Even after a good calibration other factors contribute to measurement uncertainty. We can broadly categorize the uncertainties arising from the different sources as described in the following.

- Environmental issues
    - Temperature fluctuations, vibrations and the optical noise (from photons collected by camera) contribute to overall measurement uncertainty of the WLI.
- Optical elements
    - Optical elements such as lenses, dispersive glasses cause optical aberrations and contribute to measurement uncertainty. All these factors are clubbed together in the instrument transfer function (ITF). We measure a system error data with the flat sample surface, and subtract it for all further experiments to minimize the contribution of ITF [21].
    - We use a cover glass over the sample for protection, which also contributes to uncertainty. We focus on sample cover in our analysis. We study different sample coverage (without cover, with a thin cover or a thick cover etc.), and draw some understanding on the effects of sample cover on measurement uncertainty.
- Sample surface features
    - Previous studies found that measurement uncertainty is also affected by surface roughness and surface tilt [20].
    - The contribution of surface tilt can become very pronounced at larger tilts. We generally employ WLI for studying topography of micromirror array (MMA), where mirrors are frequently tilted in various angles and directions, and so the contribution

of surface tilt in measurement uncertainty is of extreme importance in our analysis (more on MMA in chapter 1.2).

- Illumination and alignment
    - We adjust WLI with a reference surface to get best contrast. Correlogram signals with best contrast and illumination have high signal to noise ratio (SNR), which can greatly reduce the measurement uncertainty [22]. We can further reduce uncertainty for specific tilts or specific directions, by adjusting WLI with different reference surfaces. We use MMA reference surface with different patterns to adjust WLI, and study their effects in our analysis.

We can use a theoretical model of measurement uncertainty, primarily factoring in the contribution of surface tilt (but surface roughness and environmental noise are included as well), as follows

$$\delta h' = \sqrt{\frac{1}{2}\frac{<I>}{I}\left({\sigma_h}^2 + \frac{1}{12}\left[\left(\frac{\partial z_m}{\partial x}\Delta x\right)^2 + \left(\frac{\partial z_m}{\partial y}\Delta y\right)^2\right]\right) + {\delta_r}^2} \qquad \text{[20] (Eq 1.13)}$$

where $\delta h'$ is the theoretical height uncertainty,

σ_h is the surface roughness (usually standard samples will have surface roughness in specifications, it would be determined through very precise methods like Atomic Force Microscopy (AFM)),

<I> is the mean intensity of speckle pattern,

I is the intensity of an individual speckle,

δ_r is the environmental random error,

Δx, Δy are the projected pixel size on the sample,

$\frac{\partial z_m}{\partial x}, \frac{\partial z_m}{\partial y}$ are the surface gradients in x and y directions respectively, at a pixel (x,y) on 3D surface $z_m(x, y)$.

Every surface would create speckles in the reflected beam with different speckle sizes based on surface roughness. Brighter speckles usually have smaller measurement uncertainties due to photon shot noise.

1.2 Micromirror Arrays

Micromirror arrays (MMA) are part of the recently developed MEMS based optical micromachining devices. MMAs consist of 2D array of reflective square mirrors mounted on a surface as embedded components of optical MEMS. MMAs are spatial light modulators which can be programmed to create different patterns of reflected beam. They can be used for beam steering in laser scanning applications or as programmable masks in microscopy etc. They act as programmable phase-modulators with high spatial and temporal resolution.

1.2.1 Structure

We use a specific MMA (called MEMI) in our analysis which contains 256x256 square mirrors with 16µm edge length [10]. Each mirror in MMA can be independently tilted or translated by applying an electrostatic potential between the micromirror and a corresponding electrode. Following figure 1.10 shows an example of how mirror can be actuated for a hexagonal micromirror (square mirrors in MMA follow the same principle).

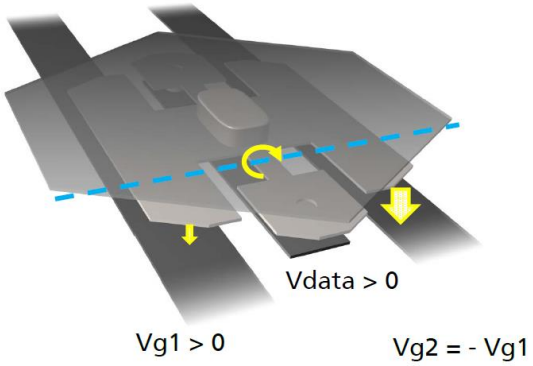


FIGURE 1.10 A hexagonal micro-mirror used for Laser Direct Imaging applications [9]

Figure 1.10 shows tilting of mirror by applying positive and negative voltage for the two different electrodes. We can translate mirror by applying same voltage with same sign on both electrodes. MMA is an analog device with more than 100 active deflection states. We can change the mirror driving voltage to arrive at different deflection states as shown in figure 1.11.

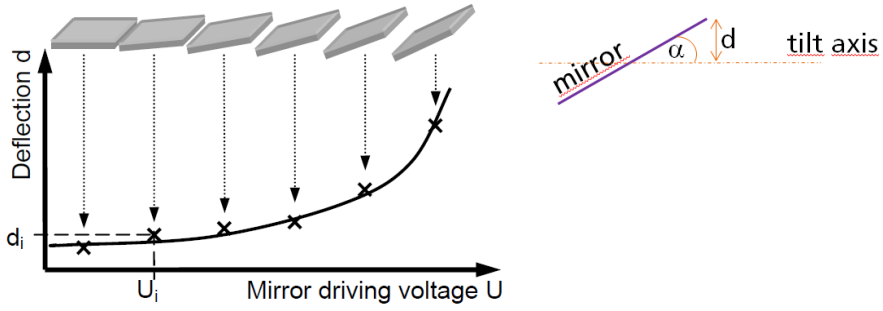


FIGURE 1.11 Mirror deflection as a function of mirror driving voltage [10]

The mirrors are hinged on to a surface as shown in figure 1.12. In order to reach targeted deflections of >350nm the torsional hinges are designed very thin. The hinges are reinforced with another layer at hinge posts and mirror posts.

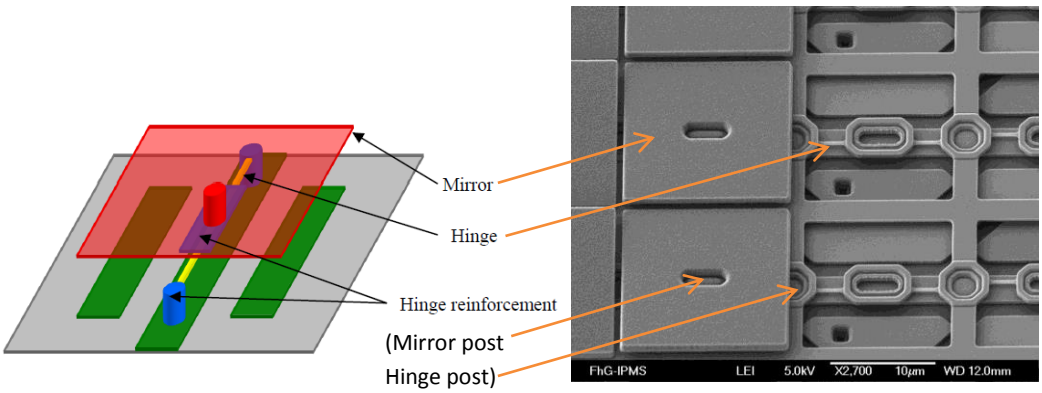


FIGURE 1.12 a. sketch of actuator layout with three layers: hinge, hinge reinforcement and mirror, **b**. SEM image of MMA in close up [10]

MMA Characterization with WLI:

MMAs can be characterized using WLI by measuring deflection as a function of voltage as shown in figure 1.11. WLI images the MMA surface topography for different mirror deflection states, an example shown in figure 1.13.

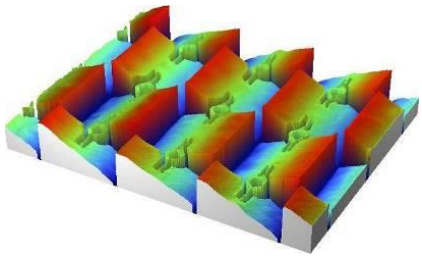


FIGURE 1.13 WLI image of deflected micromirrors (height exaggerated) [25]

WLI measurement uncertainty contributed by mirror tilt plays a significant role in the MMA characterization.

1.2.2 Applications

MMAs are useful for various applications in microscopy, lithography, metrology and many more. MMAs have mirrors which can be controlled programmatically. This offers greater flexibility in controlling light beam to achieve virtually any shape. We can create flexible patterned illumination in microscopy, create programmable masks in lithography or steer laser light in laser direct imaging [10].

Applications in lithography:

Illumination is one of the most important aspect in lithography. Controlling the shape of illumination reduces the incentive to use a separate mask layer over the sample.

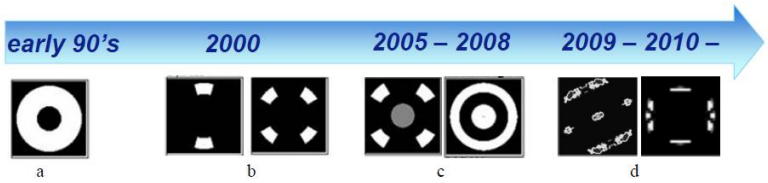


FIGURE 1.14 History of illumination source shapes [11]

Figure 1.14 shows the recent history of various patterns of illumination a. off axis, b & c. multipole illumination and d. freeform illumination. The freeform illumination can be achieved with diffractive optical elements (DOEs) as well. But DOEs have some limitations compared to fully programmable illuminator (in our case MMA). DOEs can only create a limited number of shapes and furthermore a large stock of DOEs need to be maintained and changed (inserted or removed from the microscope). Fully programmable MMA can create virtually unlimited shapes. A new shape can be achieved very fast (with programming), and thus reduces the lead-time to find a new source to few minutes.

Following figure 1.15 shows illumination shape change with four mirrors. An actual MMA may contain thousands of mirrors.

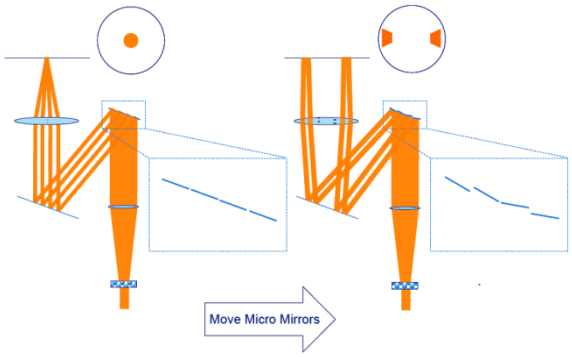


FIGURE 1.15 Changing illumination shape by tilting mirrors [11]

The figure 1.15 shows changing illumination from central positioned small convention source (left picture) to a dipole source (right picture). The mirrors are usually designed to tilt on two axes of rotation to allow reflection spot to occur anywhere in the field of view. It is important to note that there is no light lost when mirrors tilted unlike the conventional masks. With thousands of mirrors, illumination shape can be very finely tuned. And the quality of reflected beam shape is less affected even with few defective mirrors.

Applications in microscopy:

There are a number of MMA applications emerging in microscopy in the field of life sciences. For example, Structured Illumination Microscopy (SIM) uses MMA to create patterned illumination which can significantly improve optical resolution. Following figure 1.16 describes SIM briefly.

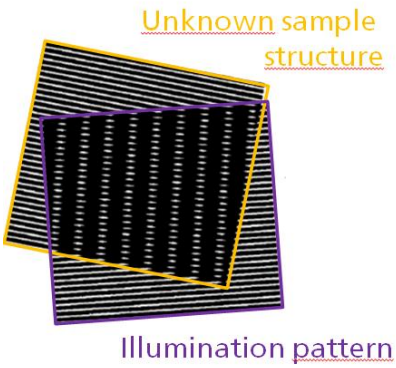


FIGURE 1.16 Moiré fringe pattern created by superposition of structured illumination and sample structure [12]

As shown in figure 1.16, in the SIM the sample is illuminated with spatially structured light which created moiré fringes containing normally inaccessible high-resolution information. With a series of such images and with the knowledge of illumination patterns, unknown structure of the sample can be resolved with much higher resolution than classical limit.

Another area which can use MMA effectively is controlled light exposure microscopy (CLEM) [23]. It uses MMA to minimize photon-induced sample damage by masking the illumination field where the light exposure is unnecessary. CLEM controls two parameters of illuminations to reduce photo-toxicity. First is to restrict the spatial region to illuminate so that other regions in the field of view are in dark, and second is to restrict the illuminating angles (i.e. the numerical aperture) at the focus in the sample so that regions outside the focus are not illuminated (as shown in figure 1.17).

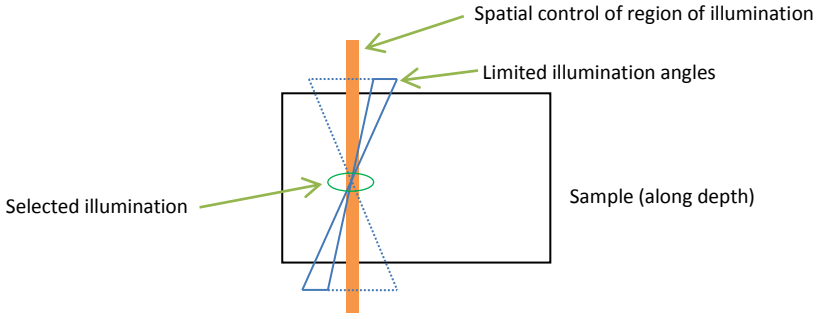


FIGURE 1.17 Selected illumination sketch on a biological sample

Chapter 2

Experimental and Analysis Methods

We use a White Light Interferometer (WLI) designed by Zygo corporation, Zygo New View 7300 (NV7300) in our experiments (as shown in figure 2.1). We have discussed about the WLI hardware in section 1.1.1, on different components and the operation of WLI. The sample holder and Zygo WLI head are separate components (they can be moved separately). We move the sample stage while placing and removing the sample. We use a joystick to control the WLI head position X, Y or Z and tilt along $\pm$X and $\pm$Y. Zygo setup is connected to a computer to process the recorded interferograms from the WLI camera [14].

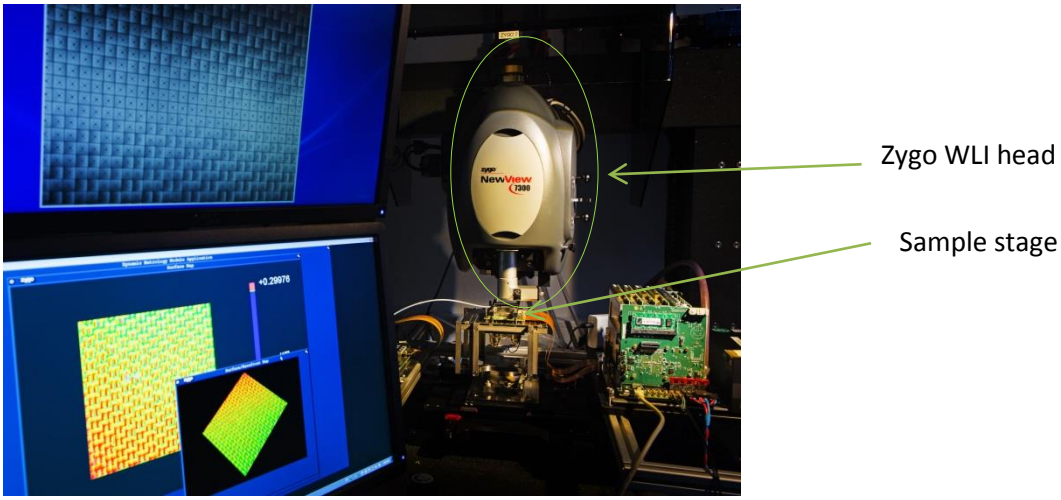


FIGURE 2.1 A picture of Zygo New View 7300 WLI used for our experiments. MetroPro software is displayed in one monitor and a live display available on a second monitor [Courtesy of Fraunhofer IPMS]

Zygo Corporation provides software (MetroPro) along with the New View WLI. MetroPro can analyze the WLI measurement data with sophisticated algorithms to derive the topography of the sample surface [24]. We can simply save the WLI raw data to a *.swl file with MetroPro and analyze at a later time (in MetroPro), or analyze with a different commercial software such as matlab [13].

MetroPro is copyright protected software which has a very extensive range of surface analysis mechanisms as shown in figure 2.2. We can view a live image of interference beam in a separate monitor. We can use MetroPro not just post processing but pre-adjustment of measurement conditions like illumination light level, and we can also give the instructions to Zygo head to run measurement, from the software itself.

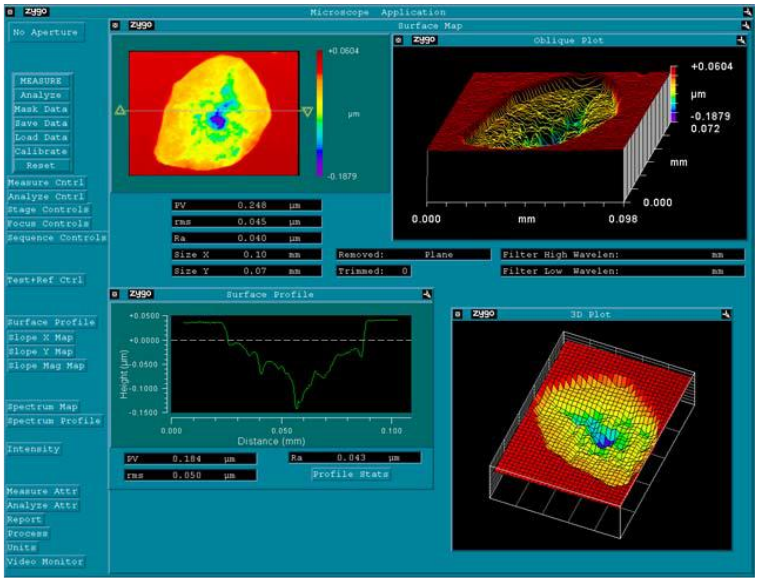


FIGURE 2.2 MetroPro surface analysis screenshot obtained from MetroPro manual [13]

Pre measurement conditions can greatly affect the measurement accuracy. Light illumination can be controlled with MetroPro but we require much more analysis. Along with MetroPro we used matlab code developed previously (by Fraunhofer IPMS team) for WLI adjustment. We performed measurements with different WLI adjustment status and analyzed the results to study the effects of WLI adjustment on measurement accuracy. The following chapter describes the various WLI adjustments that we used for our experiments in detail.

2.1 WLI Adjustment

We adjust WLI before performing measurements with the sample. The quality of measurement can significantly alter based on the adjustment. Measurement quality or uncertainty can be statistically analyzed through the correlogram analysis. We will study the effects of adjustment in our analysis.

A reference surface is used for the adjustment. We use a micromirror array (MMA) surface for our analysis. The following factors are considered for a good adjustment.

- Uniform illumination in the whole field of view (FOV).
- Best contrast on the reference MMA surface. We can achieve this when
    - a. MMA is sharply imaged on the CCD camera
    - b. Reference mirror & reference sample (MMA) are moved to achieve zero OPD between reference and sample beams [14].
- We consider wave optics of the illuminating light. We can tilt the reference surface and adjust, thus we can optimize the contrast at the specific electromagnetic field angles in the

light wave. This would help in obtaining optimum quality for measurements for the samples tilted at similar angles.

Adjusting the reference MMA surface (i.e. creating an adjustment pattern):

The MMA surface is connected via electronics to the computer and we used matlab code (developed by IPMS) to create different patterns on the surface. We can tilt mirrors on the MMA surface in different directions (X, Y or diagonal) and different angles. We can create different patterns by tilting adjacent mirrors in different directions e.g. pyramidal pattern, unidirectional chainsaw pattern etc.

For our experiments we used the following patterns.

- 0° flat surface
- 2.8° diagonal tilted mirrors in pyramidal pattern
    - 2.8° diagonal tilt of a mirror corresponds to 2° X-tilt and 2° Y-tilt for the X and Y directions respectively in the surface plane (surface plane is the XY plane)
- 2° X-tilt, unidirectional tilt along X-axis
- 3.9° X-tilt, unidirectional tilt along X-axis

Following figure 2.3 illustrates MMA with unidirectional pattern.

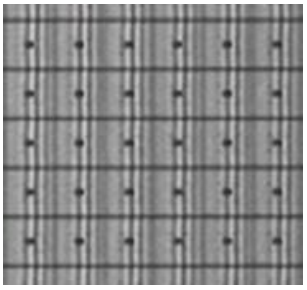


FIGURE 2.3 WLI adjustment with MMA X-tilt, unidirectional pattern [25]

Optimization parameter R:

We try to achieve the best contrast for the selected pattern. We will define the optimization parameter R by analyzing the correlograms recorded by CCD camera as described in the following.

In the CCD, each pixel acts as a separate interferometer. In each scan step we record a data point of interferogram signal for all pixels. After the full scan, complete interferograms (or correlograms) can be constructed as shown in figure 2.4. Maximum contrast is obtained for zero OPD or the center of correlogram. This contrast at zero OPD, defined as parameter WLIC, is also affected by the adjustment.

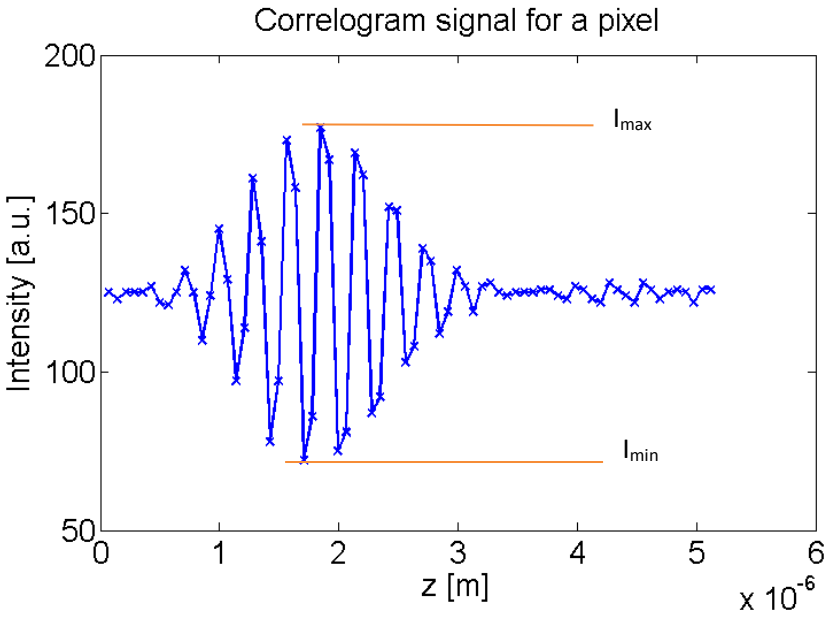


FIGURE 2.4 Correlogram recorded at a random CCD pixel [25]

We can calculate the contrast (WLIC) for each pixel as follows

$$WLIC = \frac{I_{max} - I_{minx}}{I_{max} + I_{minx}} \qquad \text{(Eq 2.1)}$$

Correlograms signal is analyzed for height topographic information. This analysis results in smaller uncertainties when the signal to noise ratio is higher (i.e. when the contrast WLIC is higher). We can take the mean WLIC of all pixels and maximize it through adjustment. We can also use the standard deviation of WLIC which represents the uniformity between pixels, and minimize it. Together we use the following parameter R to maximize for good adjustment [ref: Procedure developed by Fraunhofer IPMS].

$$\mathrm{R} = \frac{\mathrm{mean(WLIC)}}{\mathrm{std(WLIC)}} \qquad \text{(Eq 2.2)}$$

Adjusting the WLI device:

We use the joystick to position the WLI head over the MMA sample. MetroPro live image is useful to locate the sample and for focusing it. Most commonly adjusted features (F-Stop, A-Stop, reference mirror and phase-wedge) in the Zygo WLI are shown in figure 2.5.

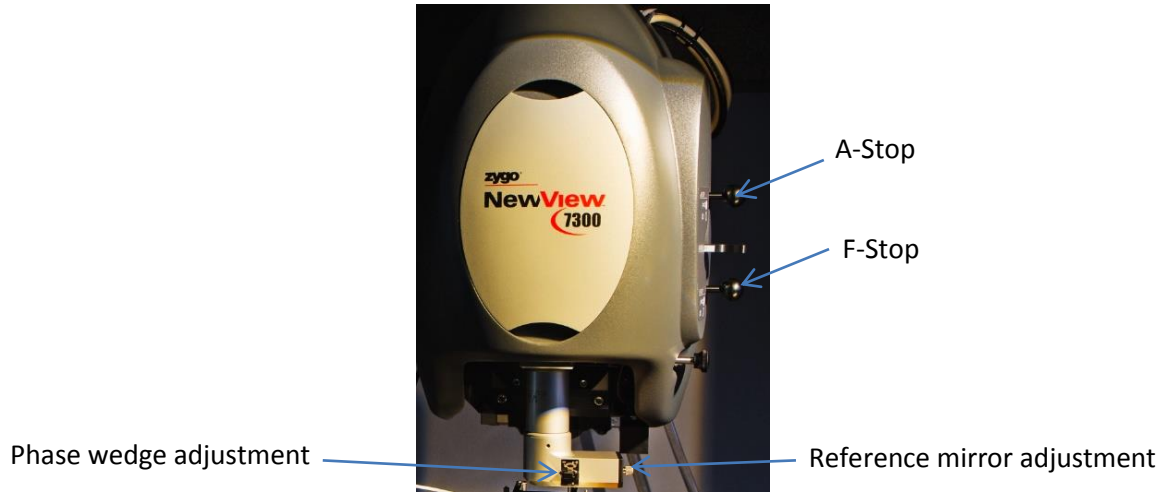


FIGURE 2.5 Zygo NV7300 common adjustment features [Courtesy of Fraunhofer IPMS]

We first set the scan length larger than the peak to valley height in the MMA sample. We then move the WLI head to focus the sample with the help of MetroPro live image. We may use F-Stop (Field Stop) as a focus aid as shown in figure 2.6. F-Stop is especially useful for focusing smooth featureless parts. The live display images the two images of sample mirror and reference mirror. When the F-stop is closed and the system is in focus the two images of sample and reference form interference fringes.

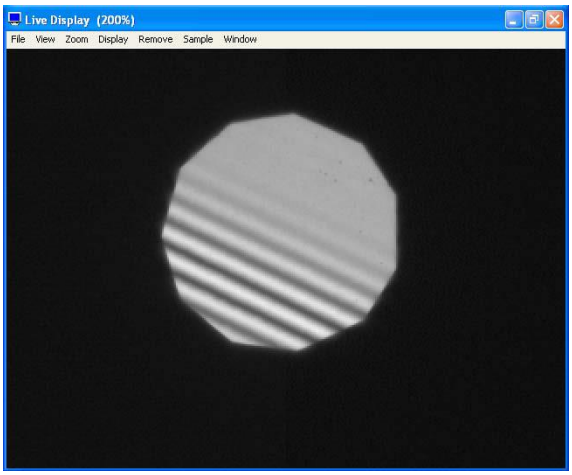


FIGURE 2.6 F-Stop closed to maximum and the system is in focus [14]

We run the matlab code and focus the MMA again for fine tuning. This time we try to achieve high contrast while the MMA is still in the focus. We need to ensure that (while adjusting) mirror edges from differently tilted mirrors have little offset. This offset usually arises because the light rays are reflected obliquely from the tilted mirror to the optical axis, and therefore refracted at a different angle in the imaging optics (see figure 1.7). By aligning the mirror edges (reducing offset) we can

ensure the same optical path lengths for different mirrors oriented differently, and thus maximize the contrast uniformly for all mirrors.

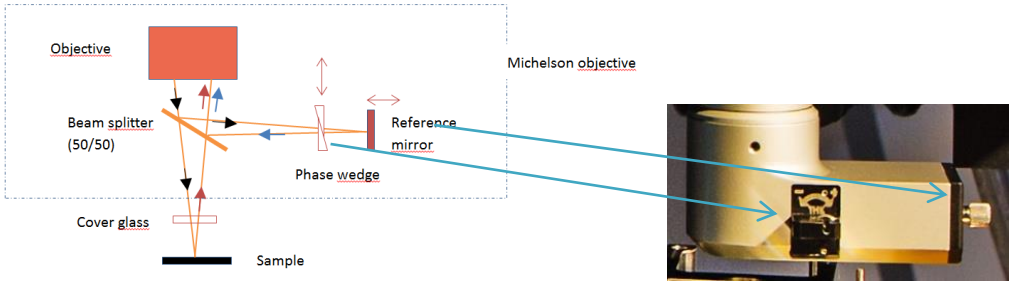


FIGURE 2.7 Reference path adjustment with phase wedge and reference mirror [25]

We move the phase wedge or reference mirror (as seen in figure 2.7), so that interference fringes are visible and visually adjust for a good contrast. We then run the matlab script where we can calculate the actual contrast. The matlab script will display the CCD image after adjustment and the optimization parameter R (eq 2.2).

We adjust the phase wedge more preferably, but we need to adjust reference mirror if any tilt is present in WLI head orientation. Now the phase wedge is moved again but slightly and the interference contrast slightly reduces. We move the WLI z-position slightly with joystick until we observe an increase in interference contrast. We run the matlab script again and check if the interference contrast parameter R increased or decreased with respect to the previous state (up/down arrow will be displayed for increment/reduction). If R increased we try to move the phase wedge again in the same direction (phase wedge screw is rotated in same direction as previous run). If R reduced we move phase wedge in the opposite direction. We repeat this process until a maximum R is reached.

We need to control the illumination as well to achieve best interference contrast. We use A-Stop (Aperture Stop) to manage the illumination light level. The light level can also be controlled with MetroPro software with either F5 key to automatically set light level or F4 key to manually adjust within a dialog window. A-Stop controls the maximum angle of incidence of illumination i.e. reducing aperture with A-Stop would result in smaller set of illumination angles. We try to change to A-Stop and run the matlab script and check the contrast parameter R. We repeat this process until we get the aperture size that gives best interference contrast.

We use the same setup, which we used for WLI adjustment, for the measurements with actual sample. We keep the reference mirror, phase wedge adjustment along with the microscope objective same. We used the same light level as well. We used different sample coverage for some of our experiments, in which case we used the same coverage for the adjustment surface as well [ref: Procedure developed by Fraunhofer IPMS].

2.2 Samples

We are using WLI for analyzing smooth planar mirror surfaces; primarily we use it for characterizing micromirror array surfaces. We used two sample surfaces for our analysis.

- Silicon carbide (SiC) mirror standard with a surface roughness of 1.25 angstrom. Rms value of 1.25 Å roughness was derived from a 1 millimeter circumference scan using a Heterodyne Optical Profiler (tested and certified by General Optics, Inc.).
- MEMI micromirror array (see section 1.2.1) containing 256x256 square mirrors and each mirror with 16 µm edge length. The MEMI mirrors can have deflections reaching above 350 nm (or 2.5°), which enables an operation in the target wavelength range between 240 nm and 800 nm [10].

We used SiC mirror standard to study measurement uncertainty of WLI for an ideal very smooth sample. We then extended our analysis to the specific case of MEMI surface. We study the effects of surface tilt on WLI measurement uncertainty.

SiC mirror:

We place the SiC mirror in the sample stage and tilt the WLI head in steps from 0° to 5°. At each tilt we run the WLI scan from MetroPro software and we save the measurement data to a *.swl file. We repeat the scans 20 times at each angle and we obtain 20 swl data files, each with the size of $\sim 200\ MB$ recorded over full field of view.

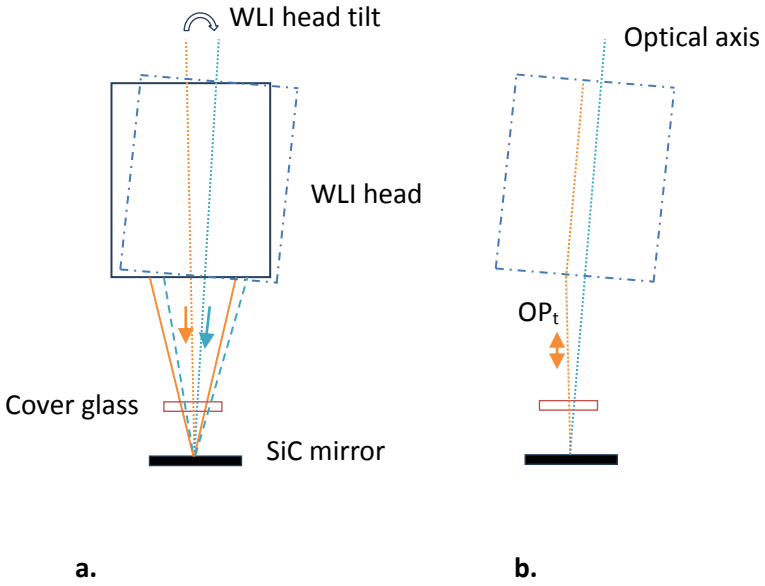


FIGURE 2.8 a. WLI head tilt with respect to sample surface normal
b. Optical path of central ray

We can see from figure 2.8a that when WLI is tilted, the incidence beam path is shifted. The central ray in the beam (central ray is the one which retraces its path) will have larger optical path (OP_t) when tilted as seen in figure 2.8b. We need to refocus after each tilt to see the interference fringes within the field of view.

We process the *.swl files in a matlab script (the script we developed for our current analysis). We obtain the height topography of SiC mirror at different tilts. Following figure 2.9 shows height topography of SiC mirror at 1.7° tilt.

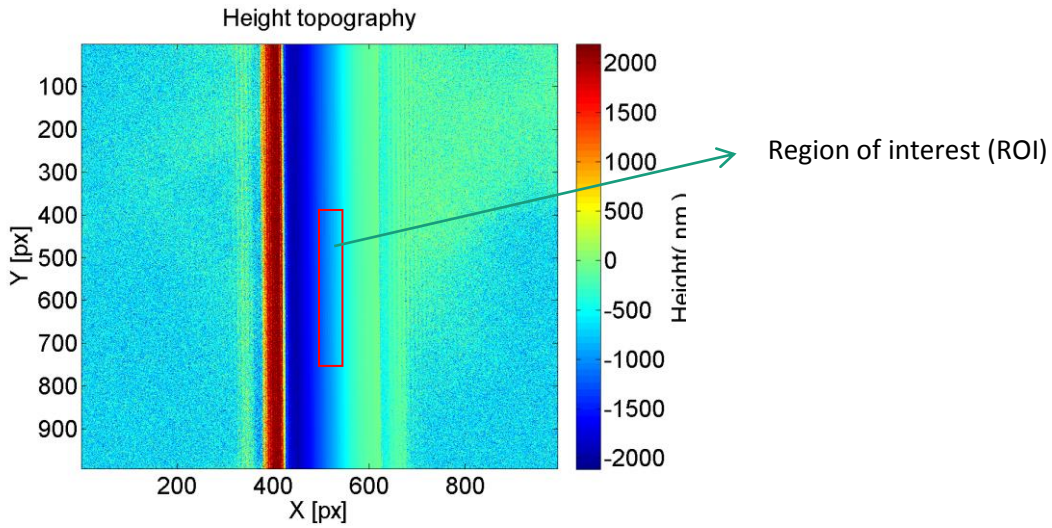


FIGURE 2.9 Height topography of SiC mirror when WLI head is tilted 1.7° along X-axis. The experiment performed without any sample cover glass

When we tilt the sample or WLI head some regions of the sample may fall outside the scan range as shown in figure 2.10. In these regions full correlograms are not formed in the scan and height analysis would not result in a correct value.

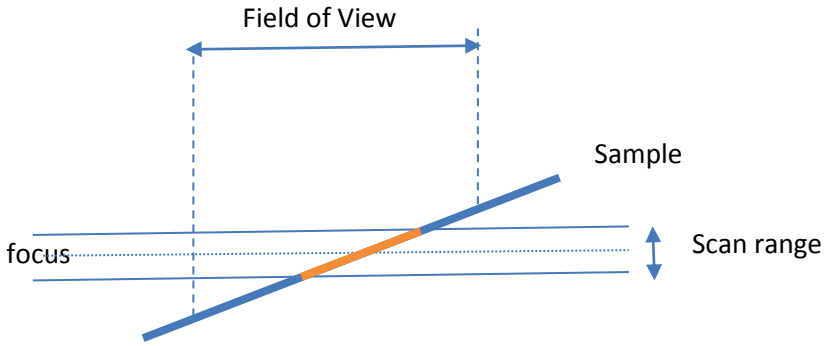
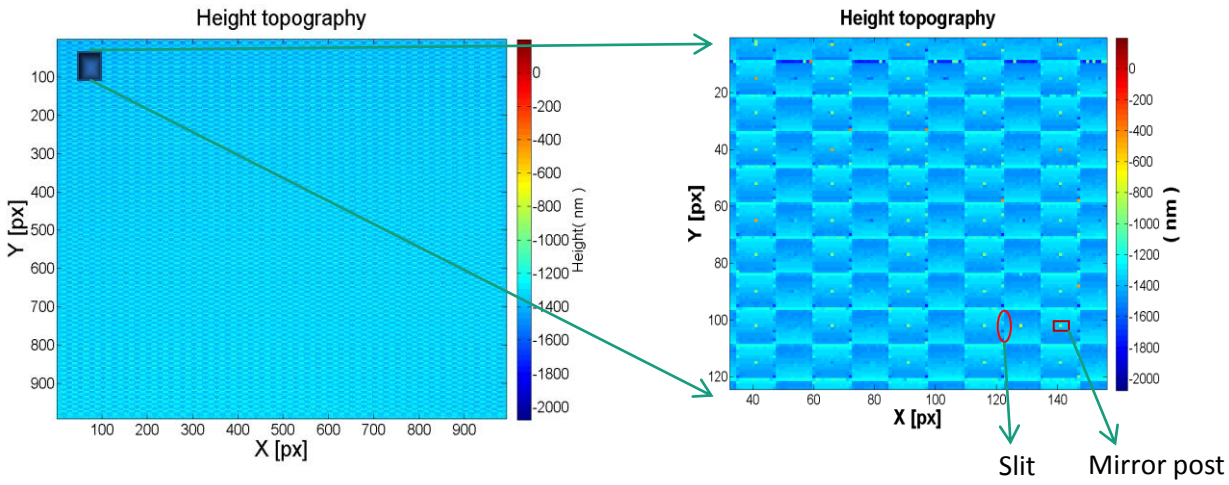


FIGURE 2.10 Tilted sample (relative to WLI head) have regions in FOV outside scan range

Figure 2.10 shows sample viewed from the tilted WLI head. We selected a region of interest (ROI) rectangular shaped within valid region containing 2500 pixels (10x250 XY-rectangle), as shown in figure 2.9. We carried out further analysis for measurement uncertainty parameters within this ROI.

MEMI surface:

We used MEMI surface as another sample for our analysis. We placed MEMI in sample stage, connected to its electronics which can control individual mirrors on MEMI surface. We use matlab script previously programmed, to control MEMI mirrors. We tilt the mirrors from 0° to 3.2° (or 0 nm to 450 nm deflection heights) along Y direction, with each Y-column of mirrors are tilted in opposite direction to its neighbor column i.e. mirrors tilted +Y,-Y,+Y,-Y,... pattern.



a. **b.**

FIGURE 2.11 a. Height topography of MEMI surface with mirrors tilted ±1.8° Y-axis,
b. Topography in small region of interest

Figure 2.11a shows the height topography we obtained with our matlab script for FDA analysis. We obtained topography for a full field of view (FOV) of 992x992 CCD pixels [14]. Figure 2.11b shows the height values in a small region of interest (ROI). We can perform full FOV analysis even for large mirror tilts (unlike the SiC mirror case, explained in figure 2.12). We divide the further analysis of MEMI surface into two parts. First part is the ROI analysis in a small ROI taken preferably close to the center of FOV i.e. close to the optical axis. And the second part is the FOV analysis to study the contribution of field of view effects in the WLI optics, to overall measurement uncertainty.

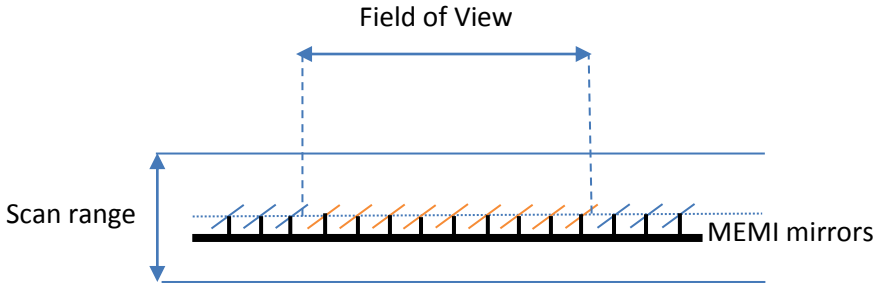


FIGURE 2.12 MEMI mirrors are in scan range even at large tilts

We can notice some regions in figure 2.11b, slits between adjacent mirrors and mirror post for support. These regions have sharp (and steep) height transitions and this could lead to multiple reflections of illuminated light. This results in very high uncertainty in the height measurement. We do not want to consider these effects to our current analysis. We can ignore the sharp regions of slits and mirror posts and analyze only smooth mirrors, using mirror recognition.

We implemented a basic mirror recognition using the image processing toolbox of matlab. The slits and post regions have large gradient in heights and the smooth mirror regions have small gradients. We used edge detection (with matlab function *edge*) to select these regions, and subtracted the edges from original height data. Figure 2.13 shows the mirrors recognized in a ROI.

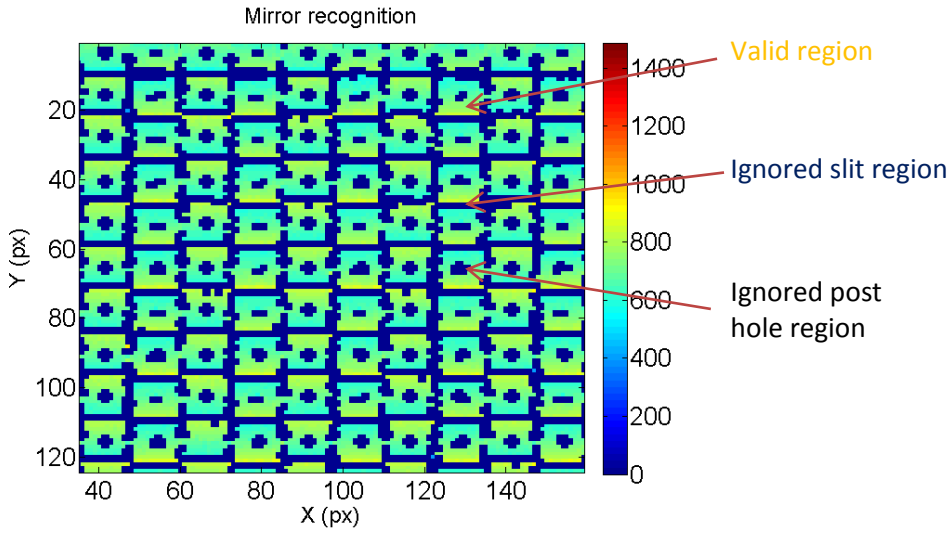


FIGURE 2.13 Recognized mirrors on MEMI MMA

We used a ROI containing 7x7 mirrors for our analysis of measurement uncertainty, which was selected close to the center of FOV. The FOV contained 78x78 mirrors in all our MEMI experiments.

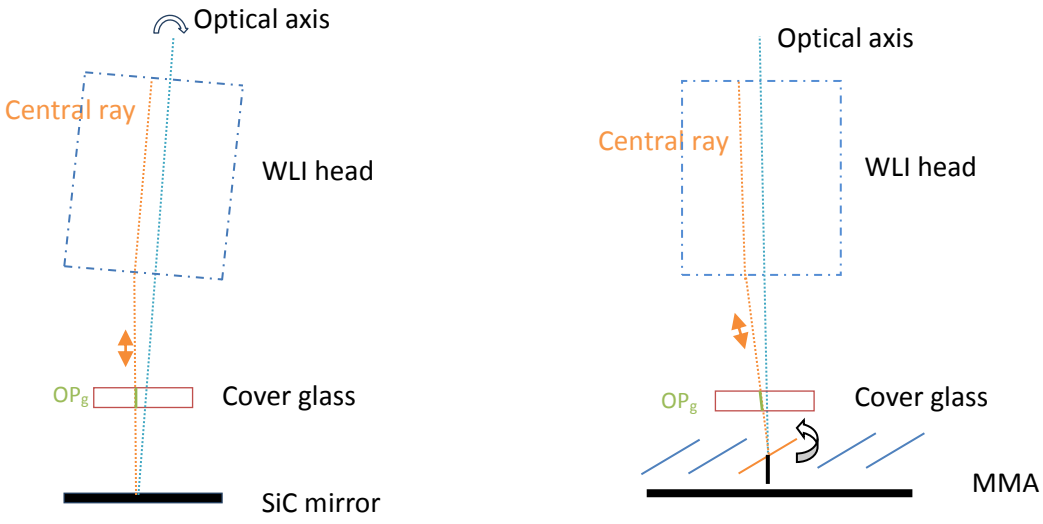
It is important to note that for the samples SiC mirror and MEMI surface we used slightly different analysis of uncertainty parameters. SiC sample is a single mirror whereas MEMI has thousands of mirrors. We considered repeatability in measurements through repeating all SiC mirror experiments 20 times, but for MEMI we used a single experiment (one experiment for each mirror tilt angle). We considered repeatability between a number of MEMI mirrors within the ROI (or FOV for field of view analysis).

2.3 Sample Cover

A cover glass is commonly placed over the sample for protection. But the cover glass (CG) might induce some additional uncertainty in the measurement. To check the CG effects, we performed experiments with the following three types of sample coverage.

- No cover over the sample. With no glass in the sample beam path we can remove the phase wedge in the reference beam path as well.
- 1.6 mm thick fused silica glass (Corning 7980). The glass is uncoated and has planarity $<\lambda/20$, wedge angle of <0.5 arc sec and rms-roughness of <0.5 nm.
- 3 mm thick fused silica glass (Suprasil 1 "248 nm Grade). The glass is uncoated and has planarity $<\lambda/20$, wedge angle of <5 arc sec.

We placed a separate cover glass (as mentioned above) for experiments with SiC mirror whereas the MEMI micromirror array was covered with a 3mm thick glass by default.



a. **b.**

FIGURE 2.14 Optical setup difference in presence of a cover glass for **a.** SiC mirror and **b.** MEMI samples

Due to the cover glass the optical system of MEMI experiments is slightly different from SiC mirror experiments especially when the mirrors are tilted as shown in figure 2.14. The tilted MEMI mirror causes the optical path in glass (OP_g) to increase compared to SiC mirror which does not change OP_g with tilt as the tilt is only in WLI head.

2.4 Raw Data Analysis

We used matlab platform for analyzing the raw measurement data. We use the MetroPro software from Zygo corporation to run the measurement and save the raw data to a *.swl file. The raw data is a 3D dataset consisting of the following

- A 2D dataset over the 992x992 camera pixels covering the full field of view (FOV).
- Interferometric intensity data from WLI scanning is in the 3rd dimension at each pixel. This data forms a correlogram signal. The scan had 135 frames over 10 µm scan range.
- We trimmed either ends of scan range and considered 72 frames. It was determined by using the ideal length of correlogram which is a characteristic of source spectrum only.

We have a large dataset of 992x992x72 size in each measurement. And we analyze correlogram signals in spatial frequency domain (FDA analysis) for each pixel separately. We use Fast Fourier Transform (FFT) in the matlab to fasten the speed of analyzing large data. We created a new function that loads the *.swl data and uses frequency domain analysis to produce height topography and phase/height uncertainties. In the following we study in detail the FDA implementation in matlab.

*Load the *.swl data*:

We use a matlab function to load *.swl file data into matlab memory. We initialize the important parameters for analysis such as number of pixels, correlogram size, scan size and scan steps either from the pre-measurement parameters (for example scan length which is set prior to measurement) or from the measurement data. The *.swl file data is loaded using memory mapping object (`memmapfile` object) which is helpful for not creating a new matlab object for our large data, and using existing memory location on the disk. This memory mapping stores the memory path to data file and we can load necessary data when required.

We trim the correlogram signal to improve the processing speed, if the scan length is much larger than the correlogram length. This should be appropriately chosen (we used double the ideal correlogram length), or should be avoided especially for the case of tilted single uniform mirror sample (SiC mirror in our analysis). It can be viewed as programmatically reducing the scan region and this can limit the valid region of height analysis (see figure 2.10) in case of tilted SiC mirror.

We implemented a way to limit the analysis to a region subset of FOV, to further improve the speed. If we have prior knowledge of the ROI that we would like to use, we can directly specify it in the

functional parameters of our function. We used full field of view FDA analysis in all our WLI measurements and specified ROI at a later stage, with the help of measured height data.

DC offset for correlogram signals:

The correlogram signal formed through interference of two beams will have a DC intensity component (see eq 1.8), given by

$$I(z) = I_0(1 + V(z)\cos(\phi(z) - \phi_0)) \quad \text{(Eq 2.3)}$$

where I_0 is the DC intensity component, $V(z)$is the envelope and is $\phi(z)$ the phase function. We can get the I_0 from measured data using

$$I_0 = \frac{I_{max}+I_{min}}{2} \quad \text{(Eq 2.4)}$$

where $I_{max} = I_0\big(1 + V(z)\big)$ and $I_{min} = I_0\big(1 - V(z)\big)$.

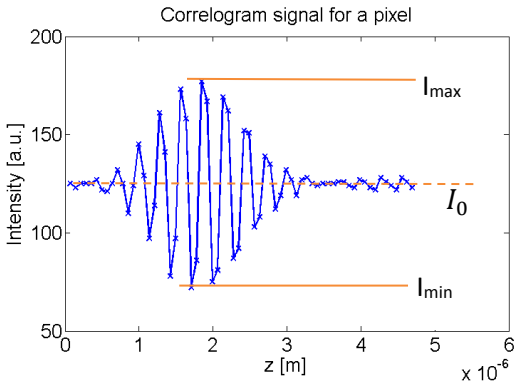


FIGURE 2.15 Correlogram signal with DC component I_0 [25]

We subtract the DC component for correlograms of all pixels as we are only interested in the phase function $\phi(z)$ in FDA analysis. I_0 may vary between pixels due to sharp surface features (like slits and post in MMA) or speckle formation. In some cases like the surface tilted to a large angle, average I_0 over pixels might even reduce, as some reflected sample beam is not collected (as shown in figure 2.16). We analyze for any significant beam loss with the tilt.



FIGURE 2.16 Sample beam collection loss for tilted sample

Fast Fourier Transform (FFT):

We use matlab function `fft` to Fourier transform (FT) the correlogram signal from z-scan distances to k-spatial frequencies. We resize the signal beforehand to the size of next power of 2 by padding extra zeroes. FFT algorithm can process much faster for signals whose size is a power of 2. The Fourier signal contains frequencies repeated twice. If K_s is the bandwidth of Fourier signal, a frequency $K_s - k$ is equivalent to $-k$, and so we can ignore frequencies more than $K_s/2$.

We obtain (spatial) frequency domain phase function $\phi(k)$ from the complex valued Fourier correlogram signal as

$$\phi(k) = \tan^{-1}\left(\frac{Im(I_F)}{Re(I_F)}\right) \qquad \text{(Eq 2.5)}$$

where I_F is the Fourier transformed correlogram signal, $Im(I_F)$ and $Re(I_F)$ are imaginary and real parts of the signal. We unwrap the phase with matlab function `unwrap` to correct for phase jumps larger than π. We define a set of physical k-values present in the light source. These we can obtain from analyzing source spectrum, by taking k-values within the bandwidth. We use the phase values within the physical k-values for further analysis. Following figure 2.17 shows a phase function from our matlab analysis.

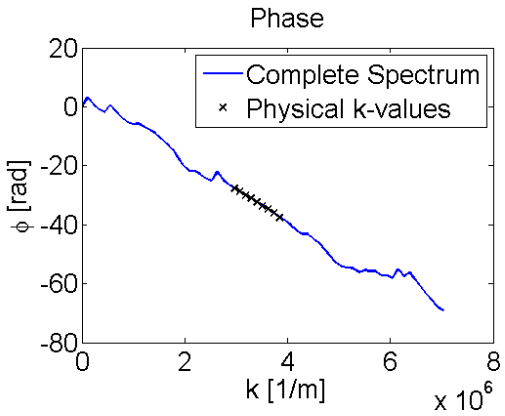


FIGURE 2.17 Phase function obtained from our matlab FDA analysis [25]

Phase analysis:

We use linear fit to phase values for the physical k-values using linear regression. We obtain height information from the slope of linear fit (see Eq 1.12). We can then stitch together height values for all pixels to obtain the topography. We initially used `for…` loops to iterate over pixel by pixel and analyzed phase sequentially. We removed `for…` loops and used matrices to analyze all pixels in parallel, which improved the processing speed significantly.

We used statistical analysis to define measurement uncertainty parameters as explained in the following sections.

2.4.1 Phase uncertainty

We can use residuals from the phase linear fit (see figure 2.17) as a measure of uncertainty

$$\phi_{res}(k) = \phi\,(k) - \phi_{fit}(k) \qquad \text{(Eq 2.6)}$$

where $\phi_{res}(k)$ are the phase residuals,

$\phi\,(k)$ is the phase signal from FDA analysis and

$\phi_{fit}(k)$ is the linearly fitted phase signal.

We fit the phase only within a range of physical spatial frequencies (determined by bandwidth of white light source spectrum). We take the root mean square (rms) of phase residuals and use it as the phase uncertainty of the corresponding pixel.

$$\delta\phi_{pix} = \sqrt{\frac{1}{\mathrm{N}-1}\sum_{\{k_{ph}\}}{\phi_{res}}^2} \qquad \text{(Eq 2.7)}$$

where $\delta\phi_{pix}$ is the phase uncertainty of a pixel,

$\{k_{ph}\}$ are the set of physical wavenumbers that are present in the light beams and

N is the size of $\{k_{ph}\}$.

We extend our analysis from pixel-wise statistics to a region of pixels or to the whole field of view. We repeat the experiments multiple times to see if the statistical uncertainties reduce when averaged over a number of experiments. We define a region of interest (ROI) on the surface for our analysis containing N_p camera pixels. For the whole field of view (FOV) analysis we extend the ROI to cover all camera pixels. We repeat our experiments by N times.

We derive the mean and standard deviation (std) of the phase uncertainty ($\delta\phi$) in the ROI for N measurements as

$$\delta\phi_m = \frac{1}{N}\sum_{i=1}^{N}\left(\frac{1}{\mathrm{Np}}\sum_{ROI}\ \delta\phi_{pix,\,i}\right) \qquad \text{(Eq 2.8)}$$

$$\delta\phi_{std} = \frac{1}{N}\sum_{i=1}^{N}\left(\sqrt{\frac{1}{\mathrm{Np}-1}\sum_{ROI}\left(\delta\phi_{pix,\,i} - \overline{\delta\phi_i}\right)^2}\right) \qquad \text{(Eq 2.9)}$$

where $\delta\phi_m$ is the mean phase uncertainty and $\delta\phi_{std}$is the standard deviation. We first evaluate the mean and standard deviation of phase uncertainty over the ROI, and then average these statistical values over N repeated measurements.

2.4.2 Height uncertainty

We can derive the height uncertainty for a pixel from phase uncertainty using eq 2.6 and eq 1.12.

$$\delta h_{pix} = \frac{\delta\phi_{pix}}{4\pi\Delta k} \qquad \text{(Eq 2.10)}$$

where Δk is the spacing between spatial frequencies of the correlogram FT signal. We assume no uncertainty in the determination of spatial frequency (k).

We can derive the height uncertainty (δh) for all pixels, with mean and std in the ROI and over N measures, as the following.

$$\delta h_m = \frac{1}{N}\sum_{i=1}^{N}\left(\frac{1}{\mathrm{Np}}\sum_{ROI} \quad \delta h_{pix,\ i}\right) \qquad \text{(Eq 2.11)}$$

$$\delta h_{std} = \frac{1}{N}\sum_{i=1}^{N}\left(\sqrt{\frac{1}{\mathrm{Np}-1}\sum_{ROI}\left(\delta h_{pix,\ i} - \overline{\delta h_i}\right)^2}\right) \qquad \text{(Eq 2.12)}$$

2.4.3 Measured Roughness

We use the known information that we use plane mirror samples in all our experiments and we define a new statistical parameter named Measured Roughness (MR) to describe planarity. The measured roughness parameter determines the roughness of the plane sample surface as measured from our experimental conditions and our analysis methods.

Before calculating MR we corrected the height data for system error. System error is the uncertainty caused by WLI optical elements, cover glass and photon shot noise etc. We averaged the 20 height measurements at 0 deg surface tilt, and we subtracted a plane from this to adjust for any tilt (a small tilt may still exist even when adjusted to 0 deg tilt). We use this as the system error data and subtract it from all 20 measurements at all tilt angles. We used different system error data for different WLI adjustments.

We derive the measured roughness (MR) as follows. Initially we fit a plane to the height data in the ROI. We will take the residuals from the plane fit and derive their root mean square (rms) value, and we denote this by the measured roughness of the sample in the ROI. We take the mean and standard deviation of MR over N repeated measurements.

$$MR_m = \frac{1}{N}\sum_{i=1}^{N} MR_i \qquad \text{(Eq 2.13)}$$

$$MR_{std} = \sqrt{\frac{1}{\mathrm{N}-1}\sum_{i=1}^{N}(MR_i - \overline{MR})^2} \qquad \text{(Eq 2.14)}$$

Comparisons with theory:

We use the theoretical height uncertainty (from Eq 1.13) and try to fit our experiments with different tilts, covers and adjustments. We do not focus our analysis on speckles and assume that $\frac{<I>}{I} = 1$. We assume our samples are uniformly planar (i.e. no curvature or discontinuities) surface and hence have a constant $\delta h'$ for all pixels. We will try to fit to our experimental analysis with the theoretical model (in later discussions).

Chapter 3

Results and Discussion

We studied the measurement uncertainty in detail through various experiments. We did experiments with different surface tilts, WLI adjustments and different sample coverage. We used two surfaces, a SiC mirror standard and a MEMI MMA. Our goal is to minimize the measurement uncertainty for various MMAs that we are using at IPMS. The experiments we performed are presented in the following.

Comprehensive list of Experiments:

Table 3.1 List of experiments we did at IPMS SLM laboratory

Sample	Tilt	Sample Cover	WLI alignment	Date
1. SiC standard	**0 to 5°** **Repeat 20 times at each angle**	**No CG**	**MMA 0°** **MMA 2.8° DIAG (Pyramid)**	**07.06.2016** **05.08.2016**
		1.6 mm	**MMA 0°** **MMA 2.8° DIAG (Pyramid)**	**06.06.2016** **29.06.2016**
		3 mm	**MMA 0°** **MMA 2.8° DIAG (Pyramid)** **MMA 2° X-tilt (unidirectional)** **MMA 3.9° X-tilt (unidirectional)**	**28.06.2016** **25.05.2016** **28.06.2016** **29.06.2016**
2. MMA MEMI	**0 to 3.2° (unidirectional)** **+Y,-Y,+Y,-Y,…**	**3 mm**	**MMA 3.2° (bidirectional)**	**12.05.2016**

Table 3.1 shows the experiments we did with SiC mirror and MEMI samples with different tilts, sample coverage and WLI adjustments. We used 7.5X magnification objectives for all MEMI experiments and 10X magnification objective for all SiC mirror experiments. We used 1X zoom in the Zygo WLI. We performed experiments in a clean room (class 10) with temperature regulated around 23$\pm$1 °C. Our Zygo NV7300 has an LED light source operating at a mean wavelength 570 nm. We used a scan range of 10 µm in all our experiments. The CCD camera recorded interferograms (correlograms) over 992x992 pixels.

3.1 Tilted SiC Standard

We calculate the four uncertainty parameters that we defined (refer section 2.4) using matlab for all the experiments shown in Table 3.1, which are

- Height uncertainty mean and std ($\delta h_m \; and \; \delta h_{std}$) and
- Measured Roughness mean and std ($MR_m \; and \; MR_{std}$).

We investigate these four uncertainty parameters for different tilts, adjustments and sample coverage.

3.1.1 Aberrations

Optical elements in the WLI device like the objective, zoom lens and including sample cover, causes aberrations in the measurement data.

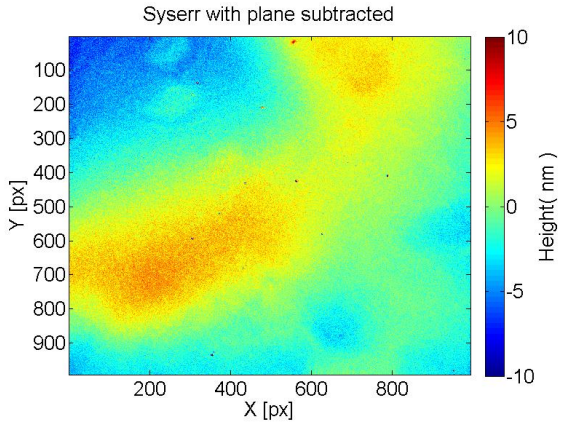


FIGURE 3.1 Aberrations in SiC mirror height measurement data

Figure 3.1 shows aberrations in the measured height data for SiC standard experiment with 1.6 mm CG and WLI adjusted with MMA 2.8° diagonal tilt. We derived the aberrations as system error (syserr) data, by averaging height data at 0° WLI tilt, and removing a plane surface from averaged height data. We remove the plane surface from heights, as we cannot perfectly adjust the WLI head

to 0° tilt, and by removing plane surface we remove any residual tilt. When we change the sample cover or when we focus WLI head in a different region on the SiC mirror, we obtain a completely different aberration profile. We subtract the syserr data from the height data, and use the corrected heights for further analysis.

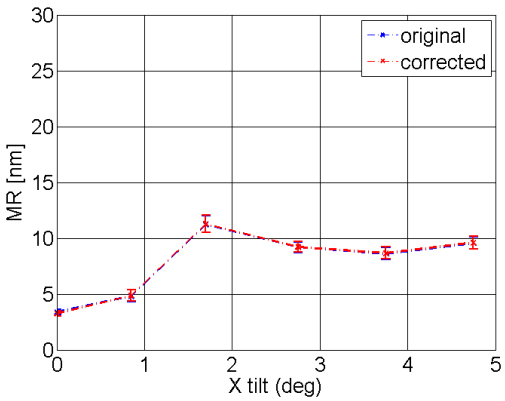


FIGURE 3.2 Measured roughness (MR) with and without aberration correction

Figure 3.2 shows the measured roughness (MR) errorbars, with original and syserr corrected height data. This figure shows results for SiC standard experiment with 1.6 mm CG and MMA 2.8° diagonal adjustment (same as figure 3.1). We can observe not much improvement in MR after correcting the syserr/aberration data. We are able to correct only height data in our analysis, and so we can only check for improvements only in the measured roughness (MR) (as shown in figure 3.2). Height uncertainty (δh) is derived from the phase analysis of correlograms, and to correct δh from aberrations we would require phase information of aberrations.

3.1.2 WLI Adjustment

We used different WLI adjustments with SiC mirror sample as shown in Table 3.1. In the following, we compared results with the sample coverage, to find the contribution of different WLI adjustments to the measurement uncertainty.

No Cover:

The following no sample cover experimental results are done with the following two types of WLI adjustments.

- Adj 1 : MMA 0° and
- Adj 2 : MMA 2.8° diagonal.

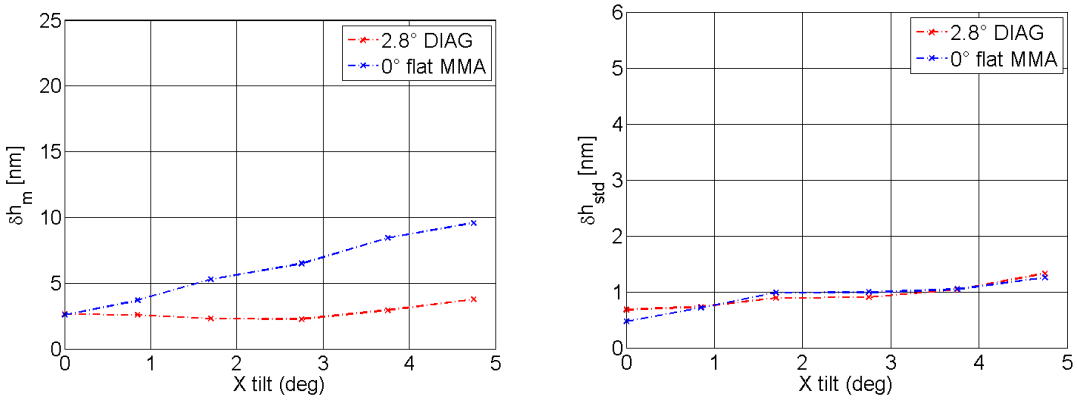


FIGURE 3.3 a. Mean height uncertainty (δh_m) and **b.** Std in height uncertainty (δh_{std}) for different tilts, adjustments and no sample coverage

Figure 3.3a shows mean height uncertainty (δh_m) as a function of different WLI adjustments. We can see from the figure 3.3a, that Adj-1 has height uncertainty (δh_m) gradually increasing with the tilt and it has become nearly 4 times from 0° to 5°. And δh_m is higher at all tilts for Adj-1 compared to Adj-2. We can also observe that in case of Adj-2, δh_m is minimum when the WLI head tilt is close to 2°, which is same as the X-tilt of MMA mirrors when WLI was adjusted (2.8° diagonal tilt corresponds to 2° X-tilt + 2° Y-tilt). We can observe reduction in uncertainty by using a special adjustment (Adj.2 is better than Adj.1), and moreover we can specifically target to reduce uncertainty at a certain tilt (Adj.2 has minimum close to 2° tilt and Adj.1 has minimum at 0° tilt).

Figure 3.3b shows height uncertainty std (δh_{std}) as a function of different WLI adjustments. δh_{std} remains nearly same for both adjustments and increases with tilt. δh_{std} is the standard deviation of height uncertainty between pixels, averaged for 20 measurements. It represents the repeatability between pixels. If field of view effects are too strong, then the uncertainty raises towards the edge pixels of the region, and thus increases δh_{std}. Figure 3.3b implies field of view effects (caused by optical setup) are increasingly predominant with the increase of tilt, but they are not affected so much by different WLI adjustments.

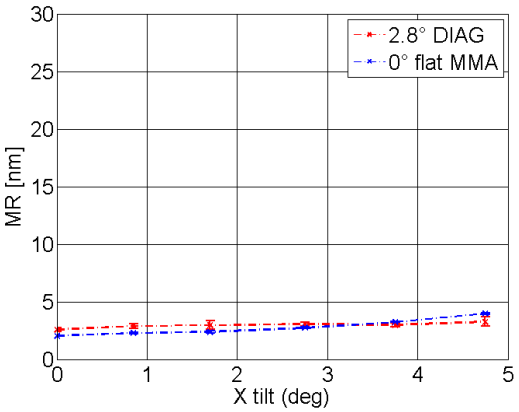


FIGURE 3.4 Measured roughness errorbars for different tilts, adjustments and no sample coverage

Figure 3.4 shows Measured roughness errorbars (MR_m and MR_{std}) as a function of different WLI adjustments. Measured roughness has very small standard deviation for both the adjustments at almost all tilts. MR_{std} is the std of MR between the 20 measurements and represents the repeatability of measurements. Mean measured roughness (MR_m) varied very little between the adjustments or between different tilts.

With no sample cover, MR plots show that the measurements are highly repeatable between experiments and the mean MR values are more or less constant.

Sample coverage with 3 mm thick glass (3mm CG):

We used a 3 mm thick cover glass with WLI adjustments as shown in Table 3.1. The results here are presented for the following adjustments.

- Adj 1 : MMA 0°,
- Adj 2 : MMA 2.8° diagonal,
- Adj 3 : MMA 2° unidirectional,
- Adj 4 : MMA 3.9° unidirectional.

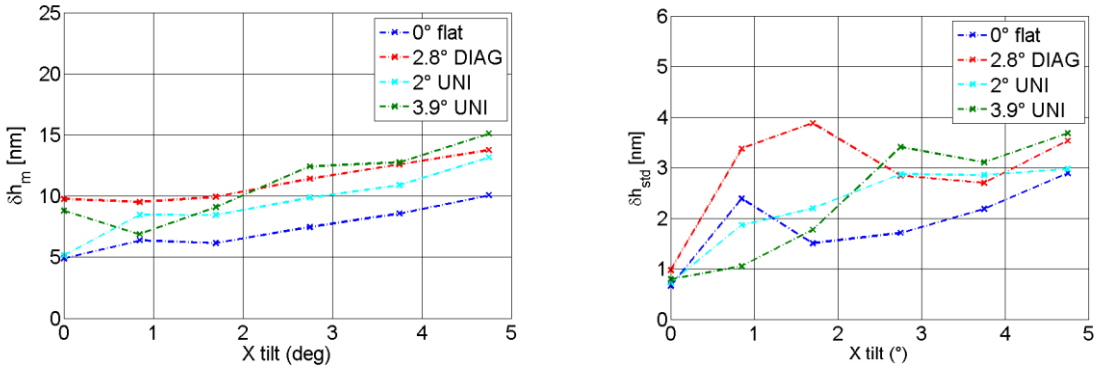


FIGURE 3.5 a. Mean height uncertainty (δh_m) and **b.** Std in height uncertainty (δh_{std}) for different tilts, adjustments and 3 mm CG

Figure 3.5a shows mean height uncertainty (δh_m) as a function of different WLI adjustments. Adj-2 has δh_m atleast 50 % more than the Adj-1 at all tilts. This result is completely opposite to the δh_m result with no cover sample (see figure 3.3a). The cover glass results (figure 3.5a) are not as expected (we expected δh_m to reduce for Adj-2 and Adj-3). A reason for this anomaly could be due to differences in optical setups for measurements with SiC standard and adjustment with MMA (see figure 2.14). In addition Adj-3 has lower uncertainty than Adj-2 although both corresponds to same tilt in X-direction (2.8° DIAG tilt is equivalent to 2° X-tilt + 2° Y-tilt). This implies that the illumination light field angles adjusted to the same direction as the measurement (X-direction) can generate lower uncertainty in measurements. Adj-4 has the largest δh_m at large tilts even though WLI is adjusted to get best results at 3.9°.

Figure 3.5b shows height uncertainty std (δh_{std}) as a function of different WLI adjustments. δh_{std} or the repeatability over the region is best for Adj-1. And Adj-3 has lower δh_{std} than Adj-2 i.e. the quality of measurement is better for Adj-3, similar to the findings from figure 3.5a. Adj-4 has the largest δh_{std} at larger tilts.

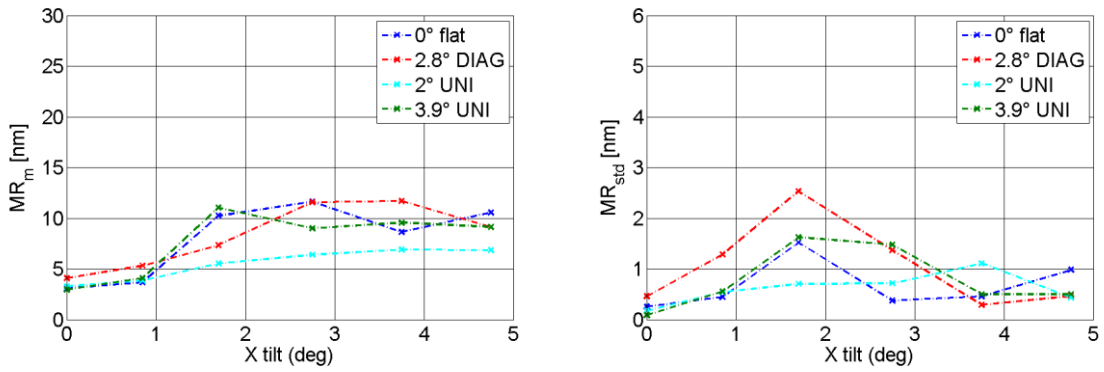


FIGURE 3.6 a. Mean measured roughness (MR_m) and **b.** Std in measured roughness (MR_{std}) for different tilts, adjustments and 3 mm CG

Figure 3.6a shows measured roughness mean (MR_m) as a function of different WLI adjustments. Adj-3, with light field angles aligned in same direction for both adjustment and sample measurements, has the lowest MR_m (or the best quality). MR_m results for Adj-1, Adj-2 and Adj-4 do not vary too much from each other.

Figure 3.6b shows measured roughness std (MR_{std}) as a function of different WLI adjustments. Adj-3 has the better repeatability between experiments compared Adj-1/2/4 i.e. better quality of measurement for Adj-3.

The results for measured roughness (figure 3.6) are quite different from the height uncertainty results (figure 3.5). MR is minimized when WLI is adjusted with Adj-3 whereas δh is minimum for Adj-1. δh is a measure of residual from phase-spatial frequency linear fit, whereas MR is a measure of deviation of fit slope from actual value (see figure 2.17). The deviation in slope is only limited by residual but does not directly dependent on it, and so the δh and MR are not fully correlated to each other.

3.1.3 Sample Cover

We used three types of sample coverage in our experiments.

- No cover glass (CG)
- 1.6 mm CG
- 3 mm CG

Following results are presented for the three sample coverage and WLI adjusted with MMA 2.8° diagonal tilt.

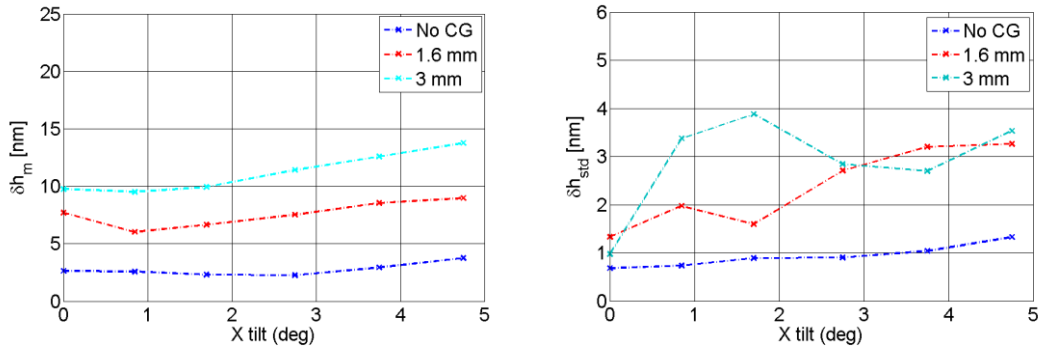


FIGURE 3.7 a. Mean height uncertainty (δh_m) and **b.** Std in height uncertainty (δh_{std}) for different tilts and No/1.6mm/3mm CG

Figure 3.7a shows mean height uncertainty (δh_m) as a function of different sample coverage. Height uncertainty (δh_m) is least when no cover is used over the sample. And δh_m increased with the thickness of cover glass (*3mm CG* has larger uncertainty than *1.6mm CG*). For practical purposes covering sample with a glass is preferred for safety. A cover glass with smaller thickness should be used in order to minimize the measurement uncertainty.

Figure 3.7b shows std in height uncertainty (δh_{std}) as a function of different sample coverage. We can see that the repeatability over pixels (or small δh_{std} value), is best for *no CG* measurements and worst for *3mm CG* measurements. A general increasing trend in δh_{std} with the tilt can also be observed for all sample coverage. Field of view effects combined with cover glass effects (like dispersion, optical aberrations) would give rise to large std in height uncertainty over the region of interest (ROI), in case of *'with CG'* measurements.

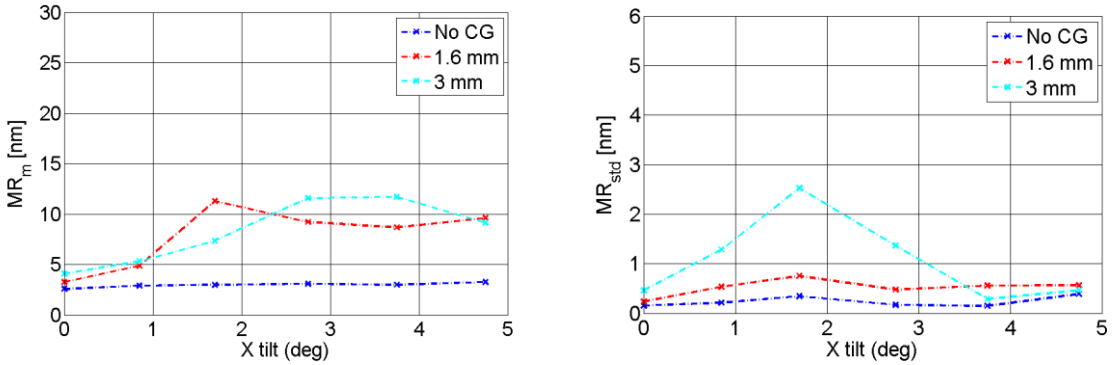


FIGURE 3.8 a. Mean measured roughness (MR_m) and **b.** Std in measured roughness (MR_{std}) for different tilts and No/1.6mm/3mm CG

Figure 3.8a shows measured roughness mean (MR_m) as a function of different sample coverage. Measured roughness is smallest for no CG measurements and increased when a cover glass is present (1.6mm/3mm CG). MR_m increased with the tilt in case of CG measurements (1.6mm/3mm)

but did not change significantly for no CG measurements. Between the *1.6mm* and *3mm CGs* we can see no significant difference in MR_m values.

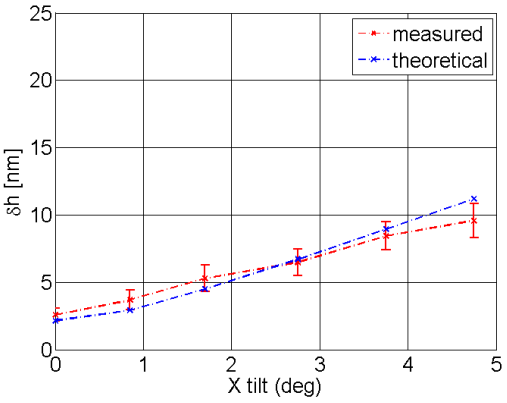
Figure 3.8b shows measured roughness std (MR_{std}) as a function of different sample coverage. Repeatability between 20 measures is best for *no CG* measurements (MR_{std} is least), and worst for *3mm CG* measurements. MR_{std} for *3mm CG* is especially worse at a tilt close to 2° (similarly δh_{std} is worse close to 2°as seen in figure 3.7b), which may be due to external factors like mechanical fluctuations in WLI while scanning.

3.1.4 Theoretical Estimations

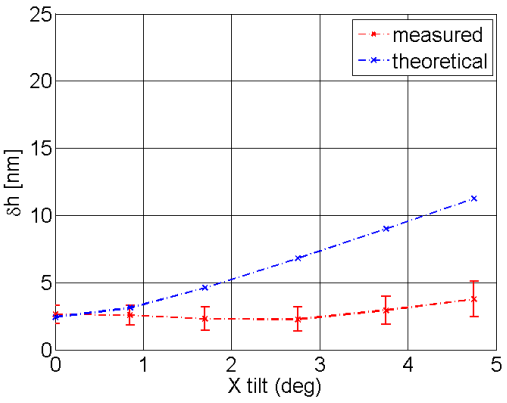
We compared our results of height uncertainty with the values derived from theory (see Eq 1.13).

$$\delta h' = \sqrt{\frac{1}{2}\frac{< I >}{I}\left({\sigma_h}^2 + \frac{1}{12}\left[\left(\frac{\partial z_m}{\partial x}\Delta x\right)^2 + \left(\frac{\partial z_m}{\partial y}\Delta y\right)^2\right]\right) + {\delta_r}^2}$$

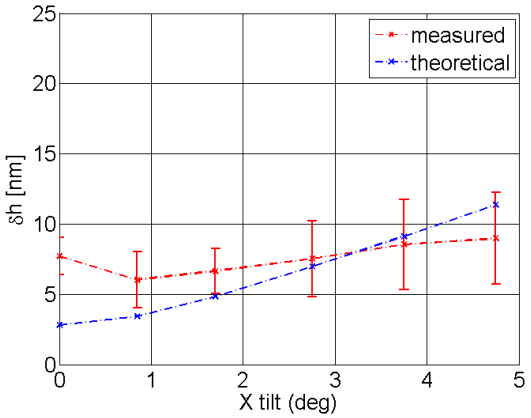
where $\delta h'$ is theoretical height uncertainty, δ_r is the environmental random error whose value was found using step height standard (for our Zygo NV7300 WLI device it was 1.6 nm). σ_h is the surface roughness which we found using mean measured roughness (MR_m) value at 0° tilt, and we used different σ_h value for experiments with different WLI adjustments and different sample coverage. Δx is the pixel size on the sample which we found using CCD pixel size / Magnification. We set $\frac{<I>}{I} = 1$ which is the ratio of the mean intensity of speckle pattern to the intensity of an individual speckle [20].



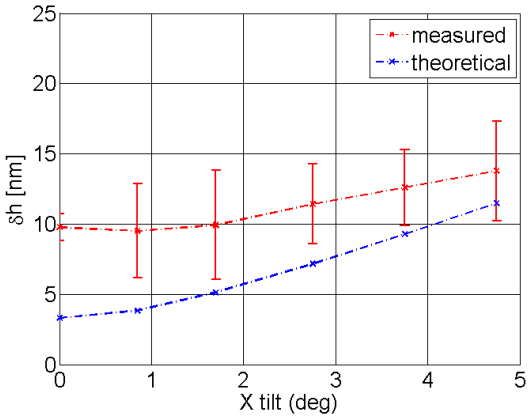
a. No CG,
adj @ MMA 0°



b. No CG,
adj @ MMA 2.8° diagonal



c. 1.6 mm CG,
adj @ MMA 2.8° diagonal



d. 3 mm CG,
adj @ MMA 2.8° diagonal

FIGURE 3.9 Theory and experimental results comparison for different sample coverage and different WLI adjustments

Figure 3.9 shows comparisons between theoretical estimations and experimental results for four different sample coverage and WLI adjustment conditions. Only figure 3.9a with no sample cover and WLI adjusted with a flat surface conforms to the theoretical estimations.

MetroPro results comparison:

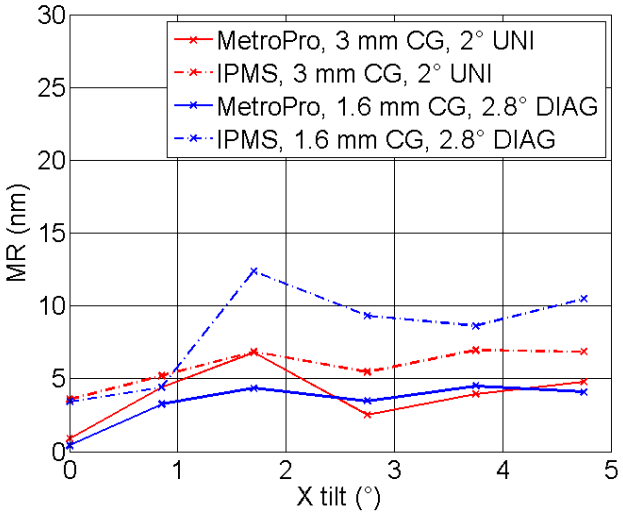


FIGURE 3.10 Measured roughness comparison between MetroPro and our IPMS results

Figure 3.10 shows measured roughness results from MetroPro and IPMS. We used rms plane residual obtained from the MetroPro topography analysis for comparison. IPMS results denote results from our implementation of simple FFT based FDA analysis in matlab. We used the first measure of the 20 measurements we did at each tilt for comparison. We compared measurements from two experimental setups, first with 1.6 mm CG and MMA 2.8° diagonal adjustment and second with 3 mm CG and MMA 2° unidirectional adjustment. In both setups we can observe MetroPro results are smaller than IPMS results. In each setup, we can also observe similar trend in MR with tilt for both MetroPro and IPMS algorithms.

3.2 Tilted Micromirrors

We used a MEMI MMA sample and tilted the micromirrors from 0 to 3.2° (or deflected mirrors from 0 to 450nm) for our experiments as noted in Table 3.1. MEMI was covered with 3mm thick glass by default. We adjusted the WLI with the same MEMI sample with mirrors tilted @3.2° in directions of +Y, -Y, +Y, -Y…. fashion.

3.2.1 Topography Measurements

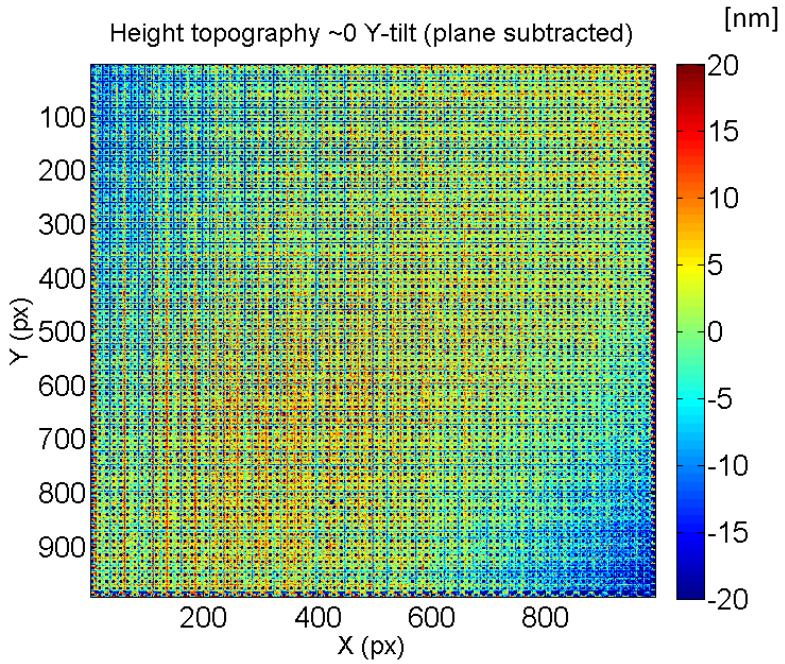
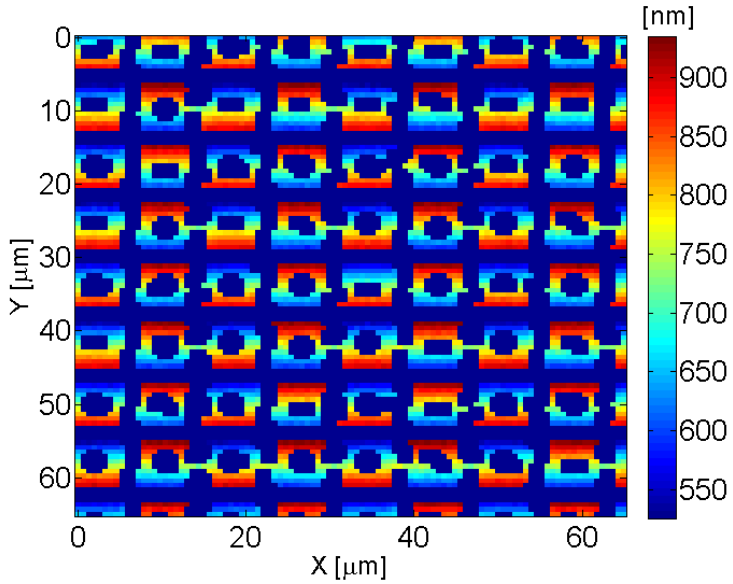


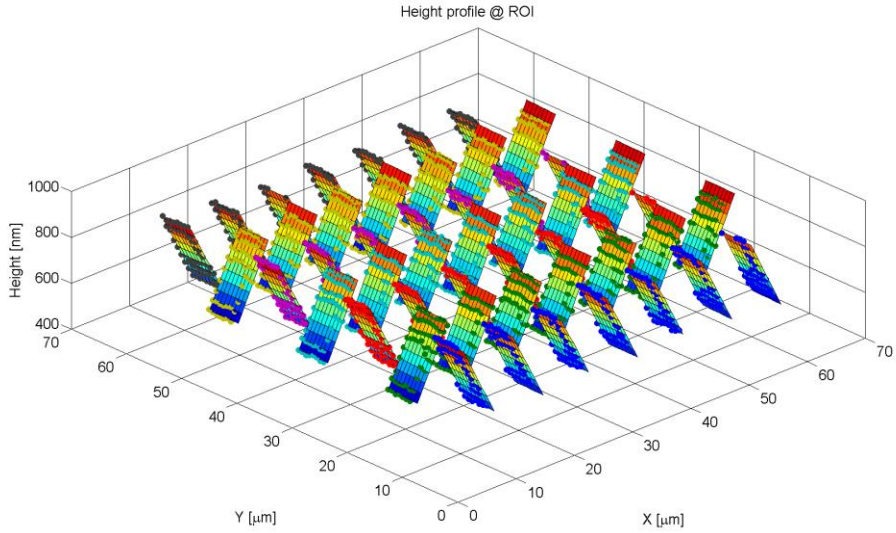
FIGURE 3.11 MEMI sample topography @ 0°mirror tilt

Figure 3.11 shows the MEMI topography in the full field of view (FOV) for 0° mirror tilt. FOV contained roughly 78 x 78 mirrors. We used FDA analysis and then mirror recognition (see section

2.2) to determine relative heights of mirrors. And we subtracted a plane (using plane fit to MEMI height data in full FOV) to correct for any slight tilt between MEMI and WLI head. We can see from the figure a bend in diagonal direction (mirrors at the top-left and bottom-right corners are at lower height than at the center), caused probably by the mechanical stress on the MEMI mirrors layer glued over MEMS surface.



a. Mirrors pixelwise



b. Mirrors fit to plane

FIGURE 3.12 MEMI in a ROI of 7x7 mirrors tilted @ 3.2°

Figure 3.12 shows MEMI mirrors in a ROI and mirrors are tilted to 3.2° in the +Y,-Y,+Y,-Y… directions. Figure 3.12a shows the height distribution pixel-wise in the ROI after the mirror recognition is run in

matlab. We can count 7x7 mirrors (only counting the full mirrors within the ROI) from figure 3.12a. We use the boundary corner pixels of 7x7 mirrors to recognize each mirror separately. Figure 3.12b shows plane fit for each of mirror height data separately. We use these plane fits to further calculate the statistic uncertainty parameter Measured Roughness (MR) for each mirror separately (unlike the SiC mirror where MR is calculated for full surface).

3.2.2 Measurement Uncertainty

We used the four statistical uncertainty parameters to describe measurements uncertainty in MEMI measurements, which are Height uncertainty mean and std ($\delta h_m \; and \; \delta h_{std}$) and Measured Roughness mean and std ($MR_m \; and \; MR_{std}$). However there are some major differences in uncertainty analysis compared to the SiC mirror experiments which are

- FOV analysis
  Unlike SiC mirror we can calculate heights for MEMI mirrors in full FOV (see section 2.2) and so we analyzed measurement uncertainties ($\delta h \; and \; MR$) in full FOV.

- Pixel-wise and mirror wise
  For MEMI sample, we calculated δh both pixel-wise and mirror-wise (by taking mean of δh over the pixels of a mirror). We calculated MR for each mirror separately.

- ROI analysis
  We also analyzed $\delta h \; and \; MR$ in a ROI to improve comparability with SiC mirror results (although results are not completely comparable as the optical setups in both cases are slightly different. See figure 2.14).

- Tilt in negative and positive Y-directions
  We have MEMI mirrors tilted in directions +Y,-Y,+Y,-Y… whereas in case SiC mirror sample WLI head is tilted in just X-direction.

- Single measurement at each mirror tilt
  We have 20 measurements at each tilt for SiC mirror sample. We have used only one measurement at each tilt for MEMI sample. We used δh mean and std over pixels in ROI/FOV and MR mean and std over mirrors in ROI/FOV.

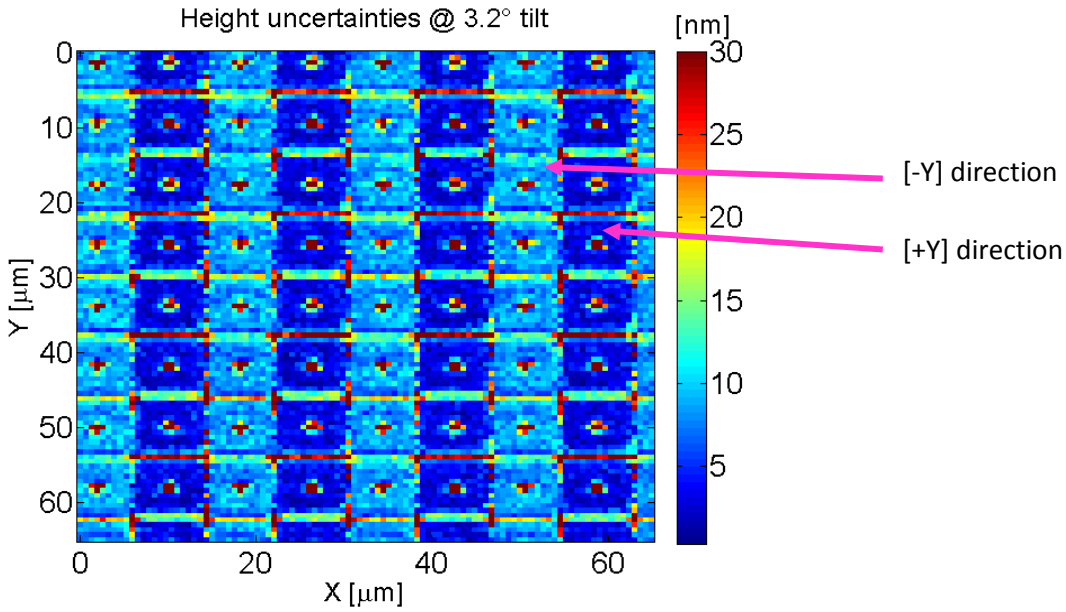


FIGURE 3.13 Height uncertainty (δh) pixel-wise in ROI

Figure 3.13 shows pixel-wise height uncertainty (δh) in a ROI over the MEMI sample where mirrors are tilted at 3.2°. We can see that δh is much higher in [–Y] direction than [+Y] direction.

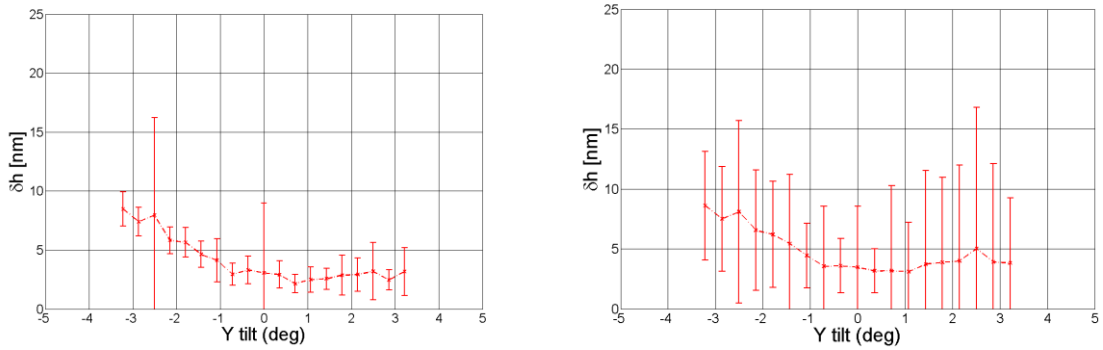


FIGURE 3.14 a. Height uncertainty (δh) errorbars over ROI (pixel-wise) **b.** δh errorbars over FOV (pixel-wise)

Figure 3.14a shows the height uncertainty errorbars (δh_m *and errorbar* δh_{std}) over the ROI as a function of mirror tilt. We can see δh_m increases much more in the [-Y] direction compared to [+Y] direction (similar to the figure 3.13). δh_{std} is very high at certain tilts, because our mirror recognition algorithm did not completely eliminate all the slit/mirror post pixels for all tilts.

Figure 3.14b shows the height uncertainty errorbars (δh_m *and errorbar* δh_{std}) over the full FOV as a function of mirror tilt. The mean δh_m values are nearly same in both figure 3.14a and 3.14b i.e. for both FOV and ROI analysis. But the δh_{std} value is much larger over FOV, meaning the height uncertainty is less uniform over the full FOV due to field of view effects caused by WLI optical elements.

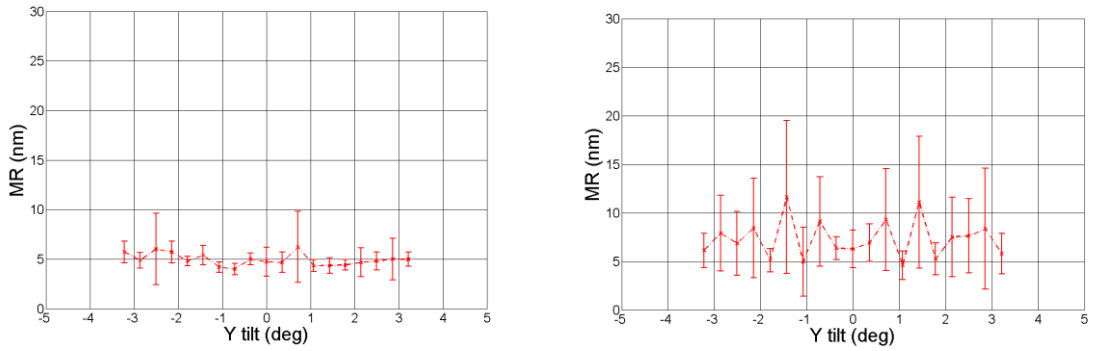


FIGURE 3.15 a. Measured roughness (MR) errorbars over ROI (mirror-wise) **b.** MR errorbars over FOV (mirror-wise)

Figure 3.15a shows the measured roughness errorbars ($MR_m \; and \; errorbar \; MR_{std}$) over the ROI as a function of mirror tilt. MR mean and std are measured over 7x7 mirrors. We can observe very small increase with the increase in tilt.

Figure 3.15b shows the measured roughness errorbars ($MR_m \; and \; errorbar \; MR_{std}$) over the ROI as a function of mirror tilt. MR mean and std are measured over 78x78 mirrors. Measured roughness mean and std values are much larger when calculated over full FOV than for the ROI. Also the MR values are not so smooth with the increase in tilt when analyzed over FOV (due to field of view effects).

3.2.3 Field of view (FOV)

We used the MEMI analysis over FOV to study the contribution of FOV effects to the measurement uncertainty.

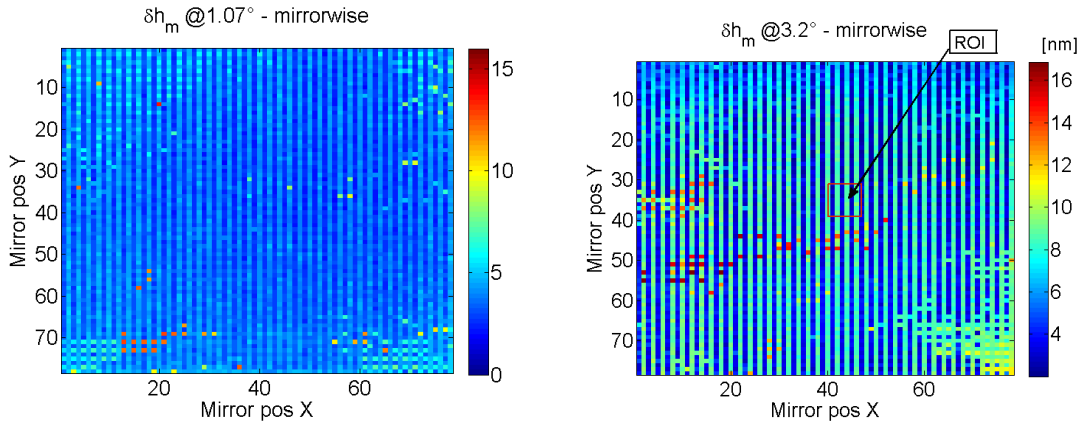


FIGURE 3.16 a. Height uncertainty (δh) mirror-wise for MEMI mirror tilts at 1.07° and **b.** mirror tilts at 3.2°

Figure 3.16a, 3.16b shows the height uncertainty (δh) distribution for each mirror (which is mean of δh of pixels belonging to a mirror) at two types of mirror tilts 1.07° and 3.2°. We can see much larger uncertainty at the FOV corners and/or edges than at the center.

We can further analyze the FOV effects by plotting mirror-wise δh as a function of radial distance of mirror from the center of FOV, as shown in the following figure 3.17.

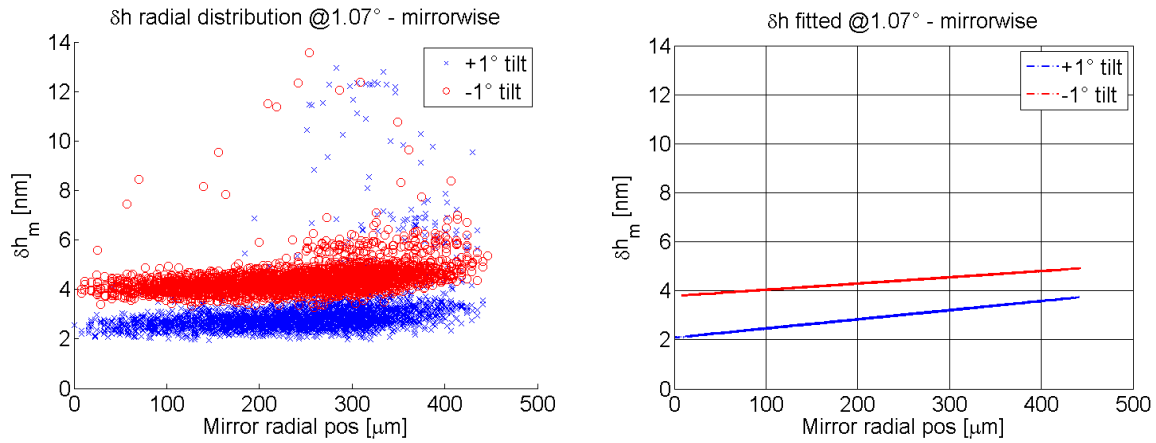


FIGURE 3.17 a. Mirror wise height uncertainty (δh) radial distributions separately for [+Y] and [-Y] tilts at 1.07° and **b.** linear fit of the δh radial distributions

Figure 3.17a, 3.17b shows the radial distribution of mirror wise δh and the linear fit of distributions, for mirror tilts at 1.07°. We have distributions separately for [+Y] and [-Y] directions and we can see that [-Y] direction has much more uncertainty similar to earlier results (see figure 3.14). We can see from figure 3.17a larger fluctuations in δh as the radial position increases. We can see from figure 3.17b that the linear fit of the distributions increases towards large radial distances i.e. edges/corners for tilts in both +Y and –Y directions. δh is at least 25% higher at the edges/corners than at the center.

Loss in sample beam with tilted surfaces:

We tilt mirrors in our analysis and tilted mirrors could cause a loss in sample beam intensity collected by the microscope objective (see figure 2.16). We analyzed the DC part of the interference intensity collected by CCD camera as shown in figure 3.18.

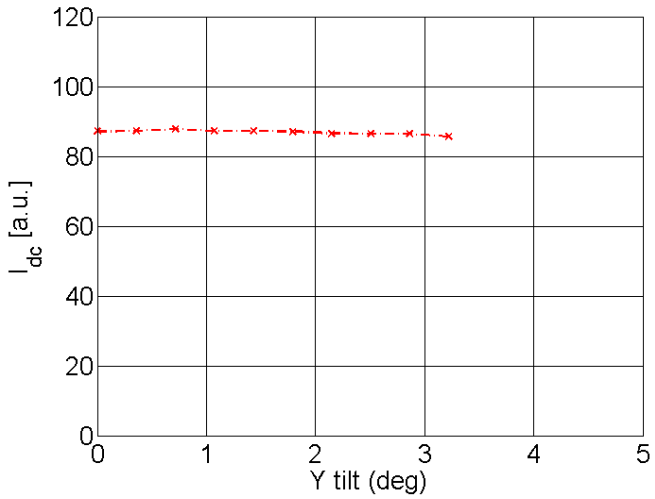


FIGURE 3.18 Mean DC intensity of correlograms recorded in FOV

Figure 3.18 shows the average DC intensity (I_{dc}) of correlograms recorded over all pixels in FOV. We can observe no considerable change in I_{dc} for the range of tilts we are using in our experiments (0 to 3.2°). This loss should be insignificant for height computations, as it does not lead to considerable loss in interference contrast.

Chapter 4

Conclusions

4.1 Prediction of Measurement Accuracy

Both the mean and spread of height uncertainty (δh) have increased with surface tilt (relative to WLI head). Measured roughness mean values (MR_m) are also increased with surface tilt, although MR_m increment is in much smaller proportion than δh_mincrement. Theoretical model produces 400% increase in height uncertainty when the surface is tilted from 0° to 4°. The theoretical model of height uncertainty is only valid when no sample cover is present and WLI is adjusted with a flat surface (i.e.0° tilt).

Measured roughness is a much more practical representation of measurement uncertainty. Measured roughness is calculated from measured height map, and it is not directly correlated to height uncertainty from phase analysis (δh). Measured roughness results do not always match height uncertainty results.

We do not need to correct for optical aberrations by WLI device. Measured roughness (both mean and std) changed very little after correcting the measured heights for optical aberrations.

We used a simple FFT based FDA analysis implemented in matlab at IPMS for our uncertainty analysis. Zygo provided MetroPro software which uses a sophisticated FDA algorithm to get heights and uncertainties [24]. MetroPro results are often more precise than IPMS algorithm but the results followed similar trends in both cases.

4.2 Influence of Sample Coverage

Height uncertainty and measured roughness are smallest when no sample cover is used. Measurement results are highly repeatable as well when no sample cover is used. Height uncertainty rises significantly for 1.6 mm/3 mm cover glasses, and it is largest for thicker (3 mm) CG. Although height uncertainty is different for 1.6 mm/3 mm, measured roughness is similar between CGs. And measured roughness is more relevant to our analysis. FFT algorithm allows to compensate for phase uncertainty, and thus gives much more precise height maps than predicted by δh. This subsequently leads to smaller measured roughness values.

Measured roughness increases when CG is present but it does not change with CG thickness. Also the measured roughness increases with tilt when CG is present but it does not change when no CG is used. It almost doubled when surface tilted from 0° to 5° for both 1.6 mm/3 mm CG. But the measured roughness does not change with tilt when no CG is used although height uncertainty

increases with tilt. This implies a simple FFT algorithm can effectively cope with larger phase uncertainties.

Theoretical model of height uncertainty (see eq. 1.13) did not fit when WLI measurements are taken with a sample cover. Theoretical model does not include contributions from CG effects. Theoretical values are much smaller than measured uncertainty values especially at smaller tilts, whereas at higher tilts they are much closer. This is due to the predominant contribution of surface tilt to the uncertainty at larger angles, whereas at small angles cover glass effects dominate. Also theoretical and measured uncertainty values differ a lot more in case of 3mm CG than 1.6mm CG, which implies that the height uncertainty contribution from CG is dependent on its thickness.

4.3 Influence of WLI Adjustment

WLI adjustment is useful to reduce height uncertainty for measurement of tilted surfaces. It was clearly observed when no sample cover was present. Height uncertainty was minimized when a specialized 2.8° diagonally tilted MMA is used for adjustment instead of a flat adjustment surface. Moreover height uncertainty was smallest when the sample is tilted 2° from WLI head. It implies height uncertainty is least when sample is oriented similar to the adjustment surface (2.8° diagonal tilt is equivalent to 2° X-tilt + 2° Y-tilt). But the measured roughness change very little either with tilt or with WLI adjustment. FFT algorithm very efficiently minimized measured roughness, and we see only small improvement with 2.8° diagonal adjustment.

When a cover glass (with 3mm thickness) is used over the sample, the CG effects further increased uncertainty. Height uncertainty minimized for flat adjustment surface, whereas the measured roughness was minimized for 2° unidirectional adjustment. Measured roughness and height uncertainty are very different parameters, and measured roughness is more preferred for our analysis. Measured roughness is minimized only for 2° unidirectional adjustment. It is larger and almost similar for flat/2.8° diagonal/3.9° unidirectional adjustments. WLI adjustment is beneficial only when adjustment surface is very similar to the sample surface. Adjustment is not effective when used with larger tilts, i.e. adjustment has upper limit of angle (Adjustment at 2° better than 3.9° unidirectional). We have to consider adjustment process for better assessment of results, which is not presented in this thesis.

Theoretical uncertainty model matches measurements only when WLI is adjusted with flat surface. Specialized adjustment with 2.8° diagonal MMA surface produces much smaller uncertainty than theoretical model when no sample cover is used. But with a cover glass, measured height uncertainty further increases, larger than theoretical values for thicker CGs. We can achieve much smaller values of uncertainty than what theoretical model predicts, by using WLI adjustment surface oriented similar to the sample to be measured.

4.4 Gain for Micromirror Characterization

Micromirrors in MMA showed predominantly higher height uncertainty in one tilt direction compared to tilt in opposite direction. This is because the WLI adjustment direction sensitive. Height uncertainty increased with the tilt similar to SiC standard results. But the measured roughness varied by much smaller amount with tilt. Although a 3 mm CG is used on top of MMA, measured roughness is almost constant unlike SiC standard (where it increased with tilt for 3mm CG). Optical setup of MMA and SiC standard is different (see fig. 2.14), tilting of CG along with SiC mirror may be responsible for increase in measured roughness with tilt.

Field of View effects were clearly visible in our results. Height uncertainty mean values remained same over the FOV but the standard deviation values are much larger. On average, mirror-wise height uncertainty at the edges of FOV is 25% larger than in the center. The increase in uncertainty away from center of optics is consistent with general optical principles.

4.5 Outlook

Height uncertainty increase with tilt is intrinsic to the WLI setup but can be minimized to a certain extent using specialized adjustment surfaces. The MMA cover should be as thin as possible, ideally leave out cover glass if possible. Theoretical model should be modified to include the CG effects.

Smaller height uncertainty could be advantageous for advanced FDA algorithms like MetroPro, since it uses phase function additionally to get much more precise height topography (see figure 3.10) [24]. MetroPro height algorithm should be used to further analyze measurement uncertainty for different sample coverage and WLI adjustments, and compare them with our results from simple FFT based FDA implementation (see figure 3.6 and 3.8).

Appendix

1. Mirror recognition code

```
I                           = heights(:,:,i);% height map
Ir                          = resds(:,:,i);% height uncertainty (δh)
I                           = I-min(min(I));
[~ ,threshold]              = edge(I, 'sobel');
thrFactor                   = .3;

% edge detection with sobel method
BWs                         = edge(I,'sobel', threshold * thrFactor);

% create square shaped structured element (SE)
ss                          = strel('square',3);
% dilate edges with SE
BWsdil                      = imdilate(BWs, ss);
% find edge pixels
indBW                       = find(BWsdil==1);
% subtract edge pixels from heightsanduncertainties
I                           = I.*~BWsdil;
Ir                          = Ir.*~BWsdil;

% distinduish edge pixels by changing value from 0 to NaN
Ir(indBW)                   = NaN;
I(indBW)                    = NaN;
```

2. FFT implementation in matlab

```
% L1 x L2 pixels in the image of full FOV
ramp            = abs(SWLI.RampSlope);      % sampling period
pixM            = 1:L1*L2;

% signal adjusted to center around zero intensity axis
signal          = double( data(pixM,:) ) - repmat(
                  double(maxi+mini)/2,1,size(data,2));

Fs              = 1/ramp;                   % Sampling frequency
T               = ramp;
L               = size(signal,2);           % Length of signal
NFFT            = 2^nextpow2(L);            % Next power of 2 from
                                               length of y

freq            = Fs/2*linspace(0,1,(NFFT/2)+1); % Frequency spectrum
                                                 repeats after Fs/2

Y               = fft(signal,NFFT,2)/L;
phase           = unwrap( angle(Y(:,1:(NFFT/2)+1)),[],2 );% unwrapped
                                                           phase
```

3. Linear fit phase-spatial frequency curve with linear regressions

```
add             = -1;

%analyze only wavelengths, which are also contained in the spectrum
of the light source!
idx             = 27-add:37+add;

%Fit an unwrapped phase function, obtained from FFT
freq            = freq(idx);
phase           = phase(:,idx);

% linear regression for phase values
% linear regression format m = X \ Y where m is the slope of Y-X
p               = [1e6*ones(length(freq'),1) freq']\phase';
phase_fit       = ([1e6*ones(length(freq'),1) freq']*p)';
```

4. Plane fit 2D height map of a mirror with multiple regression

```
height_map              = heights_cr(:,:,j,i);% height topography

% reformat pixels positions (x,y) to x1 and x2 vectors
x1                      = repmat(x_pt,size(y_pt))';
x2                      = reshape(repmat(y_pt',size(x_pt))',1,[])';

% reshape height map to a vector
y                       = reshape(height_map,1,[])';

% Plane fit with multiple linear regression
X                       = [ones(size(x1)) x1 x2];
m                       = X\y;
Y                       = double(X*m);
```

5. MEMI MMA height uncertainty – mirror wise radial distribution

```
% parameter mn: no. of mirrors along (x,y)
clear rad_s;
for j=1:mn(1)
      for k=1:mn(2)
            % radius of mirror from center
      rad_pix           = sqrt((j-mn(1)/2)^2+(k-mn(2)/2)^2);

            % radius & height uncertainty at mirror position (j,k)
      rad_s(j,k,1)      = rad_pix;
      rad_s(j,k,2)      = resds_mirror_mean(j,k,4);
      end
end
```

```
% Separate radius vs uncertainty maps for +1°, -1° directions
rad_s_even = reshape(rad_s(:,2:2:mn(2),:),mn(1)*length(2:2:mn(2)),2);
rad_s_odd = reshape(rad_s(:,1:2:mn(2),:),mn(1)*length(1:2:mn(2)),2);

% Plot radial distribution of height uncertainty for +1°, -1° mirror
% tils of MMA
figure('Visible','on','position',[300 300 750 550]);
scatter(rad_s_odd(:,1)*ms_nm(1)/1000,rad_s_odd(:,2),'bx');
hold on;
scatter(rad_s_even(:,1)*ms_nm(1)/1000,rad_s_even(:,2),'ro');
xlabel('Mirror radial pos [\mum]');
ylabel('\deltah_{m} [nm]');
title('\deltah radial distribution @1.07° - mirrorwise');
legend('+1° tilt','-1° tilt');
```

References

[1] Joanna, S. (2013). An introduction to non-contact surface metrology [PDF]. Retrieved September 25, 2016, from https://www.bruker.com/

[2] Dändliker, R., Salvadé, Y., & Zimmermann, E. (1998). Distance measurement by multiple-wavelength interferometry Mesure de distance par interférométrie à plusieurs longueurs d'onde. Journal of Optics, 29(3), 105.

[3] Wyant, J. C., & Creath, K. (1992). Advances in interferometric optical profiling. International Journal of Machine Tools and Manufacture, 32(1-2), 5-10.

[4] Leach, R., Brown, J., Jiang, X., Blunt, R., & Conroy, M. (2008). Guide to the Measurement of Smooth Surface Topography Using Coherence Scanning Interferometry; Measurement Good Practice Guide No. 108; National Physical Laboratory: Middlesex, UK, 2008. National Physical Laboratory, Hampton Road, Teddington, Middlesex.

[5] Basics of White-Light Interferometry [PDF]. Retrieved September 25, 2016, from polytec, http://www.polytec.com/

[6] Eugene Hecht, Optics, Fourth edition, ISBN 0-321-18878-0.

[7] De Groot, P. (1993). What is frequency domain analysis?. R&D Technical Bulletin, Zygo Corporation.

[8] Palodhi, K. (2013). Absolute surface topography measurement with polarisation sensitive coherence scanning interferometry (Doctoral dissertation, © Kanik Palodhi).

[9] Schenk, H., Grahmann, J., Sandner, T., Wagner, M., Dauderstädt, U., & Schmidt, J. U. (2014). Micro Mirrors for High-speed Laser Deflection and Patterning. Physics Procedia, 56, 7-18.

[10] Schmidt, J. U., Bring, M., Heber, J., Friedrichs, M., Rudloff, D., Rößler, J., et al. (2010, April). Technology development of diffractive micromirror arrays for the deep ultraviolet to the near infrared spectral range. In SPIE Photonics Europe (pp. 77162L-77162L). International Society for Optics and Photonics.

[11] Mulder, M., Engelen, A., Noordman, O., Kazinczi, R., Streutker, G., van Drieenhuizen, B., et al. (2009, December). Performance of a programmable illuminator for generation of freeform sources on high NA immersion systems. In SPIE Lithography Asia (pp. 75200Y-75200Y). International Society for Optics and Photonics.

[12] Gustafsson, M. G. (2000). Surpassing the lateral resolution limit by a factor of two using structured illumination microscopy. Journal of microscopy, 198(2), 82-87.

[13] MetroPro Reference Guide OMP-0347K [PDF]. Retrieved from Zygo Corporation, http://www.zygo.com/

[14] NewView 7200 & 7300 Operating Manual OMP-0536A [PDF]. Retrieved from Zygo Corporation, http://www.zygo.com/

[15] Osten, W. (Ed.). (2016). Optical inspection of Microsystems. CRC Press.

[16] Optical Profilers - how optical Profilers work [Web page]. Retrieved September 25, 2016, from http://www.zygo.com/

[17] Chang, G. W., Lin, Y. H., & Yeh, Z. M. (2007, January). White light interferometric profile measurement system using spectral coherence. InMOEMS-MEMS 2007 Micro and Nanofabrication (pp. 64630I-64630I). International Society for Optics and Photonics.

[18] Comparing 3D Optical Microscopy Techniques for Metrology Applications [PDF]. Retrieved September 25, 2016, from https://www.bruker.com/

[19] MENSAH, E., PEDERSEN, H., & LOKBERG, O. (2013). Measurement of Temporal Coherence of Visible CW Laser Sources Using Interferometric Methods. The African Review of Physics, 7.

[20] Liu, M., Cheung, C. F., Ren, M., & Cheng, C. H. (2015). Estimation of measurement uncertainty caused by surface gradient for a white light interferometer. Applied optics, 54(29), 8670-8677.

[21] Xie, W., Lehmann, P., & Niehues, J. (2012). Lateral resolution and transfer characteristics of vertical scanning white-light interferometers. Applied optics,51(11), 1795-1803.

[22] Wiesner, B., Hybl, O., & Häusler, G. (2012). Improved white-light interferometry on rough surfaces by statistically independent speckle patterns. Applied optics, 51(6), 751-757.

[23] Rückerl, F., Berndt, D., Heber, J., & Shorte, S. (2014, May). Photoactivation and optogenetics with micro mirror enhanced illumination. In SPIE Photonics Europe (pp. 913017-913017). International Society for Optics and Photonics.

[24] de Groot, P., de Lega, X. C., Kramer, J., & Turzhitsky, M. (2002). Determination of fringe order in white-light interference microscopy. Applied optics, 41(22), 4571-4578.

[25] Personal communication with Christoph Skupsch